JCB Journal of Cell Biology

ARTICLE

ATP13A2 facilitates HDAC6 recruitment to lysosome to promote autophagosome–lysosome fusion

Ruoxi Wang[1*], Jieqiong Tan[1*], Tingting Chen[1], Hailong Han[1], Runyi Tian[1], Ya Tan[1], Yiming Wu[1], Jingyi Cui[1], Fang Chen[1], Jie Li[1], Lu Lv[1], Xinjie Guan[1], Shuai Shang[1], Jiahong Lu[2], and Zhuohua Zhang[1,3]

Mutations in *ATP13A2* cause Kufor-Rakeb syndrome, an autosomal recessive form of juvenile-onset atypical Parkinson's disease (PD). Recent work tied *ATP13A2* to autophagy and other cellular features of neurodegeneration, but how ATP13A2 governs numerous cellular functions in PD pathogenesis is not understood. In this study, the ATP13A2-deficient mouse developed into aging-dependent phenotypes resembling those of autophagy impairment. ATP13A2 deficiency impaired autophagosome–lysosome fusion in cultured cells and in in vitro reconstitution assays. In ATP13A2-deficient cells or *Drosophila melanogaster* or mouse tissues, lysosomal localization and activity of HDAC6 were reduced, with increased acetylation of tubulin and cortactin. Wild-type HDAC6, but not a deacetylase-inactive mutant, restored autophagosome–lysosome fusion, antagonized cortactin hyperacetylation, and promoted lysosomal localization of cortactin in ATP13A2-deficient cells. Mechanistically, ATP13A2 facilitated recruitment of HDAC6 and cortactin to lysosomes. Cortactin overexpression in cultured cells reversed ATP13A2 deficiency–associated impairment of autophagosome–lysosome fusion. PD-causing ATP13A2 mutants failed to rescue autophagosome–lysosome fusion or to promote degradation of protein aggregates and damaged mitochondria. These results suggest that ATP13A2 recruits HDAC6 to lysosomes to deacetylate cortactin and promotes autophagosome–lysosome fusion and autophagy. This study identifies ATP13A2 as an essential molecular component for normal autophagy flux in vivo and implies potential treatments targeting HDAC6-mediated autophagy for PD.

Introduction

Mutations of *ATP13A2* are associated with Kufor-Rakeb syndrome (KRS), an autosomal recessive form of juvenile-onset atypical Parkinson's disease (PD) that is known as Parkinson's disease-9 (*PARK 9*; Najim al-Din et al., 1994; Ramirez et al., 2006; Santoro et al., 2011). Association of *ATP13A2* mutations with juvenile parkinsonism, early-onset PD, neuronal ceroid lipofuscinosis, and complicated hereditary spastic paraplegia was also documented (Di Fonzo et al., 2007; Lees and Singleton, 2007; Lin et al., 2008; Ning et al., 2008; Djarmati et al., 2009; Behrens et al., 2010; Mao et al., 2010; Schneider et al., 2010; Bras et al., 2012; Estrada-Cuzcano et al., 2017).

ATP13A2 encodes a lysosomal transmembrane P5B-type ATPase (Ramirez et al., 2006; Tan et al., 2011). ATP13A2 loss leads to lysosomal abnormalities (Usenovic and Krainc, 2012; Usenovic et al., 2012b; Matsui et al., 2013), impaired mitochondrial function (Grünewald et al., 2012; Gusdon et al., 2012), increased metal sensitivity (Gitler et al., 2009; Tan et al., 2011), sensitized ER stress (Ugolino et al., 2011; Radi et al., 2012), α-synuclein aggregation (Park et al., 2014; Tsunemi and Krainc, 2014), and neuronal wax-like lipofuscin deposition (Usenovic et al., 2012b; Schultheis et al., 2013) in different experimental systems. Recent studies suggest that ATP13A2 regulates autophagy (Usenovic et al., 2012a), although how ATP13A2 governs numerous cellular functions is not understood.

Impaired autophagy is implicated in the pathogenesis of neurodegenerative diseases, including PD (Levine and Kroemer, 2008; Jiang and Mizushima, 2014). Autophagy is a tightly regulated process that degrades proteins or damaged cellular organelles via lysosomes (LYSs). Aggregates or damaged organelles are first targeted and packed into membrane structures known as autophagosomes (APSs), followed by LYS fusion to form autolysosomes that degrade contents. APS formation has been intensively studied, and multiple autophagy-associated factors and related complexes are identified (Mizushima et al., 2011; Lamb et al., 2013). Molecules associated with vesicle fusion, including SNAREs, small GTPs, and phosphoinositide

[1]Institute of Molecular Precision Medicine, Xiangya Hospital and Center for Medical Genetics, Central South University, Changsha, Hunan, China; [2]State Key Laboratory of Quality Research in Chinese Medicine, Institute of Chinese Medical Sciences, University of Macau, Taipa, Macau; [3]Department of Neurosciences, School of Medicine, University of South China, Hengyang, Hunan, China.

*R. Wang and J. Tan contributed equally to this paper; Correspondence to Zhuohua Zhang: zhangzhuohua@sklmg.edu.cn.

regulators, also regulate APS–LYS fusion (Shen and Mizushima, 2014; Hasegawa et al., 2016; Wang et al., 2016). Mutations in some of these genes cause human diseases, suggesting that APS–LYS fusion is essential for completion of productive autophagy (Hasegawa et al., 2016; Wang et al., 2016; Xia et al., 2016). Recently, actin remodeling regulated by the histone deacetylase HDAC6 was shown to play an important role in promoting the fusion process (Lee et al., 2010). Nevertheless, the molecular events of APS–LYS fusion remain largely unknown.

In this study, we asked how ATP13A2 functions in pathophysiological contexts. The ATP13A2-deficient mouse developed into phenotypes resembling those of mice with autophagy gene knockout. Further experiments revealed that ATP13A2 inactivation reduced HDAC6 activity, increased cortactin acetylation, and disrupted APS–LYS fusion. ATP13A2 facilitates recruitment of HDAC6 to LYS to deacetylate cortactin and control APS–LYS fusion. Therefore, ATP13A2 inactivation impaired autophagy flux, resulting in the accumulation of insoluble proteins and damaged mitochondria, likely contributing to PD pathogenesis.

Results

Aging-dependent hepatomegaly, reduced adipose tissue mass, and accumulation of LC3-II and p62 in ATP13A2-null mice

To investigate the pathophysiology of ATP13A2, we examined ATP13A2-null mice at ages 4, 10, and 18 mo (Fig. S1 a). At 4 mo, ATP13A2-null mice were generally normal. At 10 mo, ATP13A2-null mice showed gradual loss of body weight, increased liver size, and reduced adipose tissue mass. These phenotypes further progressed to age 18 mo, with significant smaller body size, hepatomegaly, and markedly reduced adipose tissues, compared with WT littermates (Fig. 1, a, b, d, and e; and Fig. S1 b). Histological analysis revealed increased intracellular vacuolation in liver tissues and small adipocytes in adipose tissues (Fig. 1, c and f), accumulation of oil red O stain–positive lipid droplets (Fig. 1 g), and reduced glycogen deposition in liver tissues (Fig. 1 h) of ATP13A2-null mice. Inactivation of autophagy genes often shows abnormal liver growth and lipid metabolism (Komatsu et al., 2005; Singh et al., 2009; Zhang et al., 2009; Jaber et al., 2012; Ni et al., 2012; Zhao et al., 2012; Settembre et al., 2013). In ATP13A2-null mice at age 18 mo, we also detected accumulation of p62, LC3, and insoluble ubiquitinated proteins in hepatocytes compared with WT controls (Fig. 1, i–l). Immunohistology showed increased p62 and LC3 in mouse livers (Fig. S1, c–f'). Transmission electron microscopy (TEM) analysis found accumulation of APS and multivesicular bodies in ATP13A2-null hepatocytes (Fig. 1, m and n). Together, the results strongly suggest aging-dependent autophagy impairment of ATP13A2-null mice.

ATP13A2 regulates LYS homeostasis via an HDAC6-mediated mechanism

To determine ATP13A2 cellular function, we generated ATP13A2-null HEK293 and HeLa cells using CRISPR/Cas9 (Fig. S1, g and h). Immunofluorescence analysis revealed a more than twofold increase in the intensity of the LYS marker LAMP1 in ATP13A2-null HEK293 cells over parental control cells (Fig. S1, i and j). A similar observation was made in mouse embryonic fibroblasts (MEFs) generated from ATP13A2-null mice (Fig. S1, k and l). Immunoblot analysis confirmed increased LAMP2 levels in ATP13A2-null HEK293 cells (Fig. S1, m and n) and MEFs (Fig. S1, o and p). Despite LYS accumulation, activity of the lysosomal enzyme cathepsin D in ATP13A2-null HEK293 cells, ATP13A2-null mouse brain tissues, liver tissues, and MEFs was significantly decreased relative to matched normal controls (Fig. S1, q–t). TEM analysis revealed accumulation of abnormal LYS in ATP13A2-null mouse brain tissues (Fig. S2).

To our surprise, acetylation of α-tubulin was also significantly increased in ATP13A2-null HEK293 cells (Fig. 2, a and b) and in ATP13A2-null mouse liver tissues (Fig. 2, c and d) relative to their matched controls. *Drosophila melanogaster CG32000* (referred to here as *dATP13A2*) is the sole orthologue of human *ATP13A2* (Fig. 3 a). Consistently, acetylated α-tubulin was significantly higher in brain tissues of three independent *Drosophila* lines with *dATP13A2* knockdown than in control WT flies (Fig. 2, e and f; and Fig. 3, b–d). In contrast, total α-tubulin levels were comparable in ATP13A2-deficient cells and tissues and respective matched controls (Fig. 2, a, c, and e). Reintroducing human ATP13A2 into ATP13A2-null HEK293 cells or fly neurons suppressed α-tubulin acetylation (Fig. S3, a and b; and Fig. 3, c and d). The results suggest that ATP13A2 inactivation results in impaired lysosomal accumulation and increased tubulin acetylation.

HDAC6 is the prime α-tubulin deacetylase (Hubbert et al., 2002). We next evaluated HDAC6 expression in our models. We detected no difference in HDAC6 protein levels between ATP13A2-null HEK293 cells or ATP13A2-null mouse liver tissues and matched controls (Fig. 2, a and c, middle panels). To assess HDAC6 activity in ATP13A2-null HEK293 cells, we treated cells with the HDAC6 inhibitor tubacin for 16 h, released cells from inhibition by changing to tubacin-free medium, and collected cells at different time points after tubacin removal. We found that levels of acetylated α-tubulin gradually decreased after tubacin removal in WT control cells, with a half-life of 90 min. By contrast, the half-life of acetylated α-tubulin was ∼3 h after tubacin removal in ATP13A2-null cells (Fig. 2, g and h). Sirt2 is also reported to deacetylate α-tubulin (North et al., 2003). Overexpression of *HDAC6*, but not of *sirt2*, restored autophagic flux in HDAC6 knockout HEK293 cells (Fig. S3, c and d). HDAC6 knockout using CRISPR/Cas9 resulted in a marked increase in α-tubulin acetylation in HEK293 cells (Fig. S1 u). Consistently, *d*sirt2 knockdown in *Drosophila* showed little effect on α-tubulin acetylation (Fig. S3, e–g). The results suggest that ATP13A2 facilitates HDAC6 activity.

A previous study showed an ATP13A2/HDAC6 interaction in a yeast two-hybrid assay (Usenovic et al., 2012a). Immunoprecipitation analysis of HEK293 cells overexpressing ATP13A2 showed that ATP13A2 coprecipitated with endogenous HDAC6 (Fig. S3 h). Conversely, endogenous HDAC6 coimmunoprecipitated with overexpressed ATP13A2 (Fig. S3 i). We could not detect endogenous ATP13A2 because of the lack of a suitable antibody. Nonetheless, ATP13A2 likely interacts with HDAC6 in vivo, supporting the notion that ATP13A2 regulates HDAC6 activity.

To further determine functional interaction of HDAC6 and LYS, we expressed human WT HDAC6 or its deacetylase-inactive mutant (H611A) in ATP13A2-null HEK293 cells and MEFs (Zou et

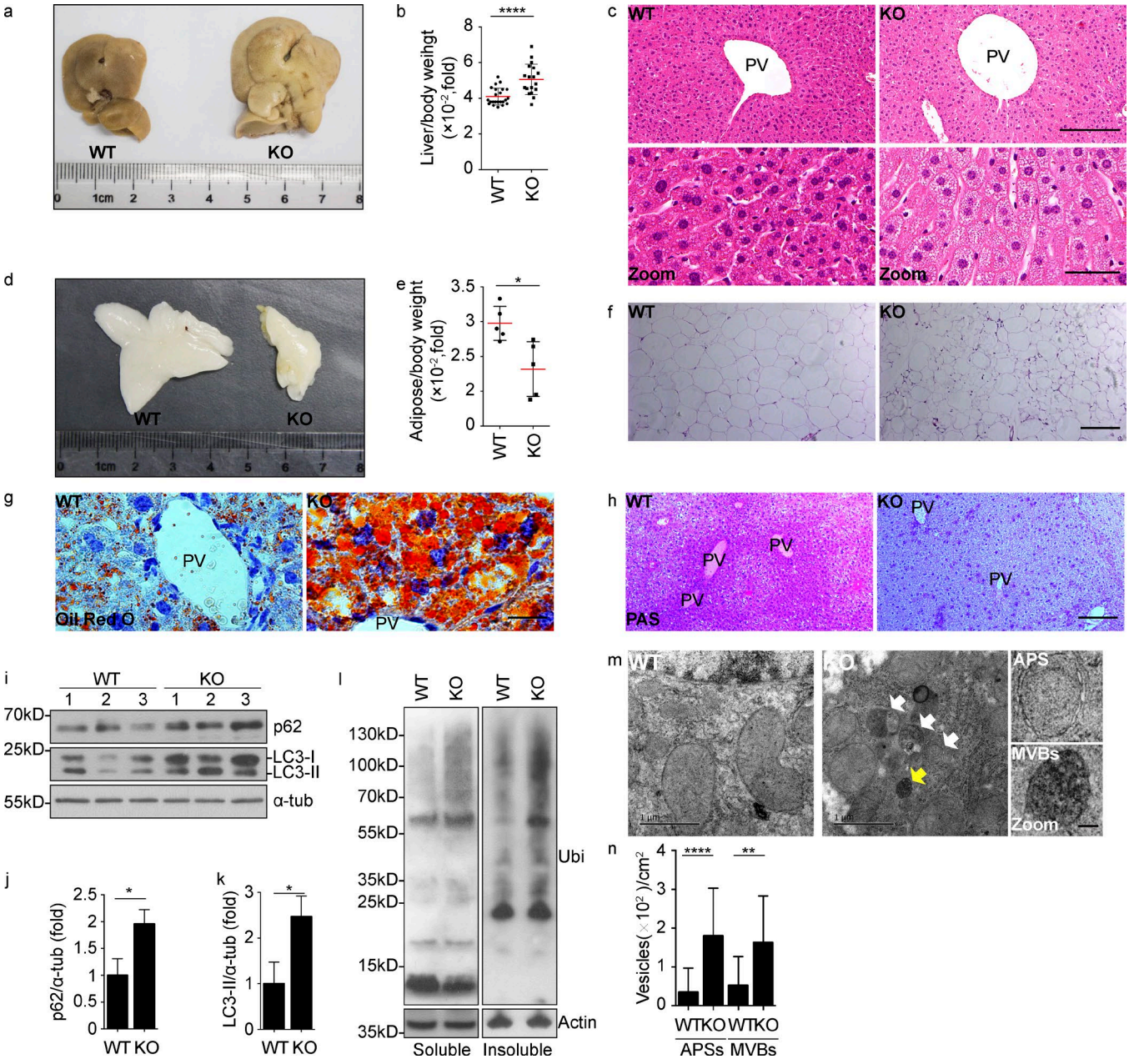

Figure 1. **ATP13A2-null mice develop autophagy impairment-like phenotypes. (a and b)** Hepatomegaly of ATP13A2-null mice. Livers of control (WT) and ATP13A2-null (knockout [KO]) mice (a) at age 16–18 mo and quantitative analysis of liver mass related to their body weight (b) are shown. ****, P < 0.0001. WT: *n* = 17, KO: *n* = 13. **(c)** H&E staining of liver tissues. Representative images of liver tissues of control (WT) and ATP13A2 null (KO) mice with H&E stain are shown. PV, portal vein. Upper panel: bar, 200 µm; lower panel: bar, 50 µm. **(d and e)** Reduced adipose tissue mass. Adipose tissues of control (WT) and ATP13A2-null (KO) mice (d) at age 16–18 mo and quantitative analysis of adipose tissue mass related to their body weight (e) are shown. *, P < 0.05. WT: *n* = 5, KO: *n* = 5. **(f)** H&E staining of adipose tissues. Representative images of adipose tissues of control (WT) and ATP13A2-null (KO) mice with H&E stain are shown. Bar, 200 µm. **(g and h)** Oil red O and periodic acid–Schiff staining. Representative images of livers of control (WT) and ATP13A2-null (KO) mice with oil red O staining (g) and periodic acid–Schiff staining (h) are shown. PV, portal vein. Bar, 20 µm (g), 200 µm (h). **(i–k)** Detection of p62 and LC3-II. Liver tissue lysates of control (WT) and ATP13A2-null (KO) mice were immunodetected for p62, LC3 (LC3-II) and α-tubulin (α-tub) (i). Quantitative analysis of p62 (j) and LC3-II (k) is shown. *, P < 0.05, *n* = 3. **(l)** Accumulation of ubiquitinated insoluble proteins in ATP13A2-null mice. Triton X-100–soluble (left panel) and –insoluble (right panel) proteins were extracted from livers of control (WT) and ATP13A2-null (KO) mice, followed by immunodetection for ubiquitin (Ubi) and actin. **(m and n)** TEM analysis of liver tissues of control (WT) and ATP13A2-null (KO) mice. Yellow arrows: APSs; white arrows: multivesicular bodies (MVBs; m). Bar, 1 µm. Higher magnification images are shown (Zoom). Bar, 0.1 µm. (n) Quantitative analysis of APSs and MVBs in relative images (2.5 × 2.5 µm² per image) is shown. **, P < 0.01; ****, P < 0.0001. WT: *n* = 36, KO: *n* = 42.

al., 2006). LYS accumulation was suppressed by overexpression of ATP13A2 or WT HDAC6, but not the HDAC6 H611A mutant (Fig. 4, a and b; and Fig. S3, j and k). Consistently, increased α-tubulin acetylation in ATP13A2-null cells was restored by overexpressing WT HDAC6, but not the HDAC6 H611A mutant (Fig. 4, c and d; and Fig. S3, l and m).

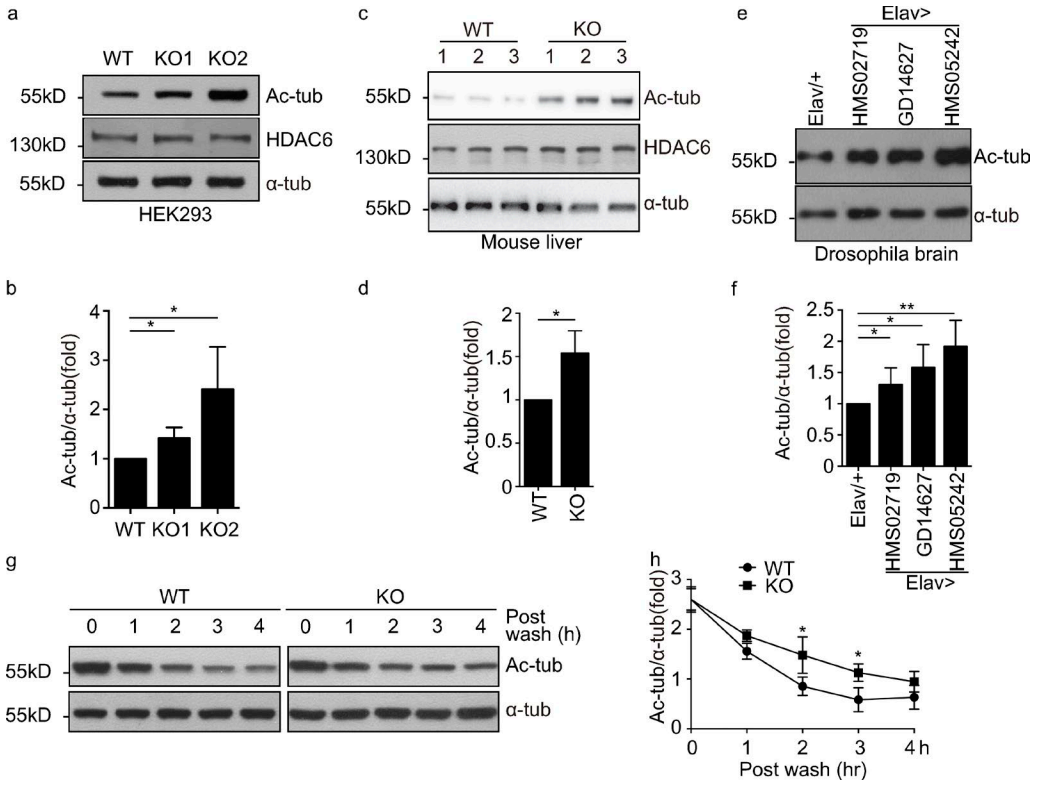

Figure 2. **Reduced HDAC6 activity in ATP13A2-null cells. (a–f)** Increased α-tubulin acetylation with ATP13A2 deficiency. Lysates of ATP13A2-null (KO) HEK293 cells (a) and mouse liver tissues (c), ATP13A2 RNAi *Drosophila* brain tissues (e) and their corresponding controls (WT) were immunodetected for acetyl-α-tubulin (Ac-tub), HDAC6, and α-tubulin (α-tub). Respective quantitation of Ac-tub is shown (b, d, and f). Two independent ATP13A2-null cell lines (a; KO1 and -2), liver tissues from three ATP13A2-null mice (c; KO 1, 2, and 3), and three independent *Drosophila* ATP13A2 RNAi lines (e, HMS02719, GD14627, and HMS05242) were analyzed. For *Drosophila*, RNAi expression was driven by elav-gal4 (e; Elav>). An elav-gal4 line served as control (e; Elav/+). *, $P < 0.05$; **, $P < 0.01$, $n = 3$. **(g and h)** Reduced HDAC6 activity in ATP13A2-null cells. ATP13A2-null HEK293 (KO) and control cells (WT) were treated with HDAC6 inhibitor tubacin for 16 h followed by tubacin removal. Cells were collected at indicated time points (post wash). Cell lysates were immunodetected for acetyl-α-tubulin (g; Ac-tub) and α-tubulin (α-tub). Relative levels of Ac-tub (Ac-tub/α-tub) are shown (h). *, $P < 0.05$, $n = 3$.

In *Drosophila*, amino acid H664 of *d*HDAC6 corresponds to residue H611 of the human HDAC6 catalytic site (Fig. 4 e). *dATP13A2* knockdown in follicle cells resulted in α-tubulin hyperacetylation, LYS accumulation, and reduced active form of the lysosomal hydrolase cathepsin B. Overexpression of WT *d*HDAC6, but not *d*HDAC6 H664A, inhibited α-tubulin hyperacetylation and LYS accumulation, and restored cathepsin B activity (Fig. 4, f and l; and Fig. S3 n). TEM analysis revealed that abnormal LYS observed in ATP13A2-null HEK293 cells were cleared by overexpression of HDAC6 (Fig. 4, m and n). Thus, ATP13A2 deficiency-induced lysosomal abnormalities are suppressed by HDAC6, suggesting that ATP13A2 plays essential roles in maintaining HDAC6 activity and normal lysosomal functions.

ATP13A2 regulates APS–LYS fusion

HDAC6 reportedly regulates APS–LYS fusion (Lee et al., 2010). We hypothesized that autophagy impairment in ATP13A2-null cells is caused by disruption of APS–LYS fusion. To test this hypothesis, we first examined colocalization of LC3 and LAMP1 in HeLa cells treated with rapamycin. 43% of LC3 vesicles are LAMP1 positive in WT cells. The colocalization was significantly reduced to <25% in ATP13A2-null HeLa cells (Fig. 5, a and b). Next, we transfected MEFs with pH-sensitive GFP-mCherry-LC3, a commonly used indicator of APS–LYS fusion (Kimura et al., 2007). Under acidic conditions marking APS–LYS fusion, GFP fluorescence is lost, leading to retention of red mCherry signals only. Nonfusing cells yield both GFP and mCherry (yellow) fluorescence. In WT MEFs, red vesicles were colocalized with LAMP1, whereas colocalization of green GFP fluorescence with LAMP1 was minimal (Fig. 5, c and d, upper panels). By contrast, yellow vesicles did not colocalize with LAMP1, whereas green and red vesicles were colocalized in ATP13A2-null MEFs (Fig. 5, c and d, lower panels). Likewise, TEM analysis revealed accumulation of double-membrane structured APS in ATP13A2-null HEK293 cells relative to their control cells (Fig. S4, a and b). The results suggest that ATP13A2 regulates APS–LYS fusion.

To further verify roles of ATP13A2 in APS–LYS fusion, we performed in vitro fusion assays in an energy-regenerating system using APS and LYS isolated from mouse livers (Fig. S4, c and d). APS–LYS fusion was observed when both vesicles were isolated from WT mice (Fig. 5 f). The fusion was effectively inhibited in buffer lacking of ATP (Fig. 5 e) or by the fusion inhibitor bafilomycin A1 (Fig. 5 g). As expected, little fusion was detected when both APS and LYS were isolated from ATP13A2-null mice (Fig. 5 h), with neither APS isolated from WT mice nor LYS isolated from ATP13A2-null mice (Fig. 5 i). Nevertheless, fusion was normal when we combined APS isolated from ATP13A2-null mice and LYS isolated from WT mice (Fig. 5 j). HADC6 inhibitor tuba-

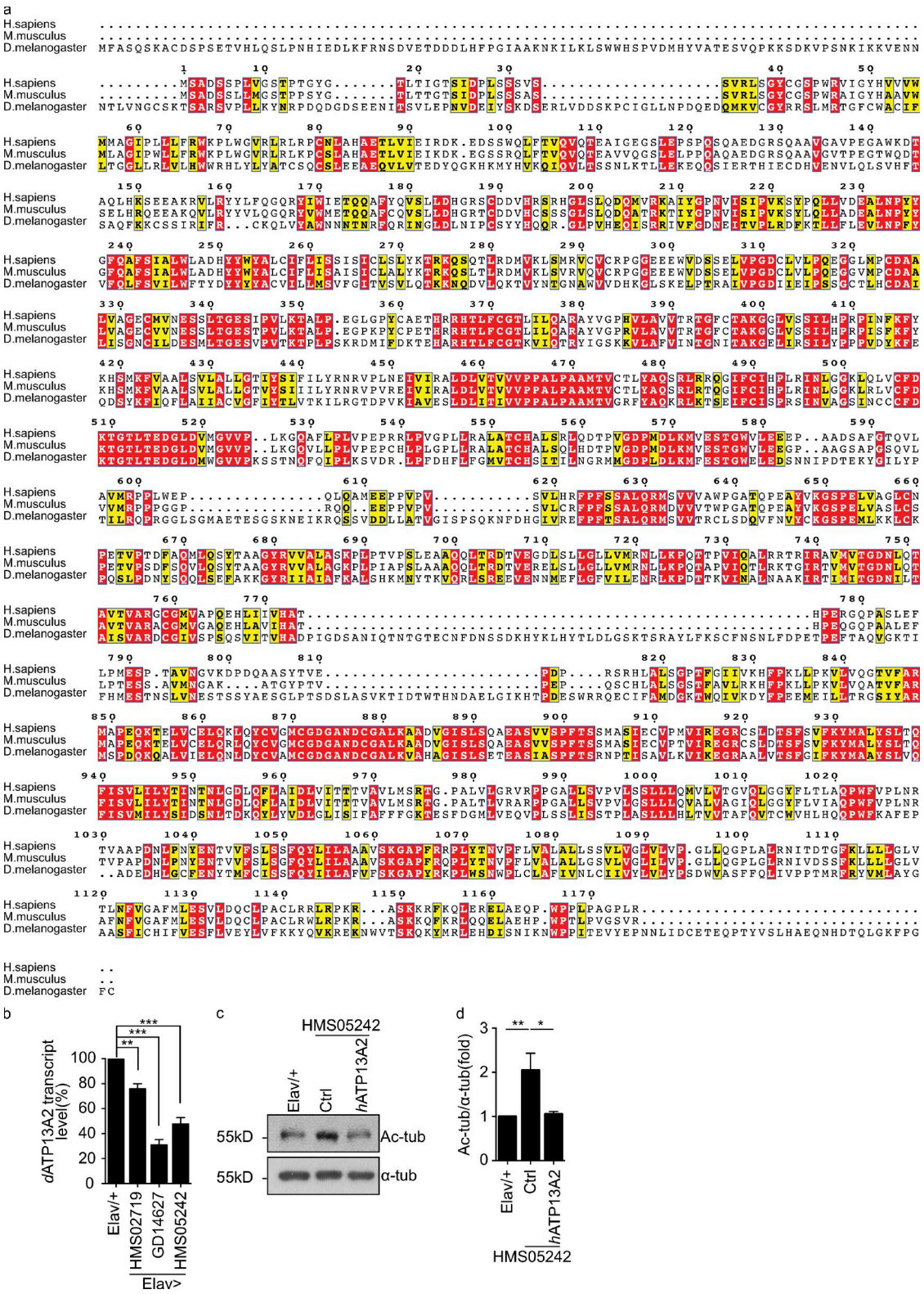

Figure 3. **Characterization of *Drosophila* ATP13A2 (*d*ATP13A2). (a)** Amino acid sequence alignment of human ATP13A2 (*H. sapiens*), mouse ATP13A2 (*M. musculus*), and *Drosophila* CG32000 (*D. melanogaster*). Amino acids in identity or similarity among the three different origins are highlighted in red or yellow, respectively. CG32000 shares 33% identity and 48% similarity with mouse ATP13A2, as well as 36% identity and 52% similarity with human ATP13A2. **(b–d)** *d*ATP13A2 knockdown results in increased tubulin acetylation. Relative RNA levels of three independent *Drosophila* RNAi lines (HMS02719, GD14627, and HMS05242) driven by elav-gal4 and a WT control harboring elav-gal4 (Elav/+) are quantified by real-time PCR (b). **, $P < 0.01$; ***, $P < 0.001$, $n = 3$. Brain lysates of flies with either elav-driven *d*ATP13A2 RNAi (RNAi HMS05242) followed by expressing human ATP13A2 (RNAi HMS05242, *h*ATP13A2) or elav-driven *d*ATP13A2 RNAi (HMS05242 RNAi; Ctrl) alone were immunodetected for acetyl-α-tubulin (Ac-tub) and α-tubulin (α-tub; c). Quantitative analysis of Ac-tub is shown (d). *, $P < 0.05$; **, $P < 0.01$, $n = 3$.

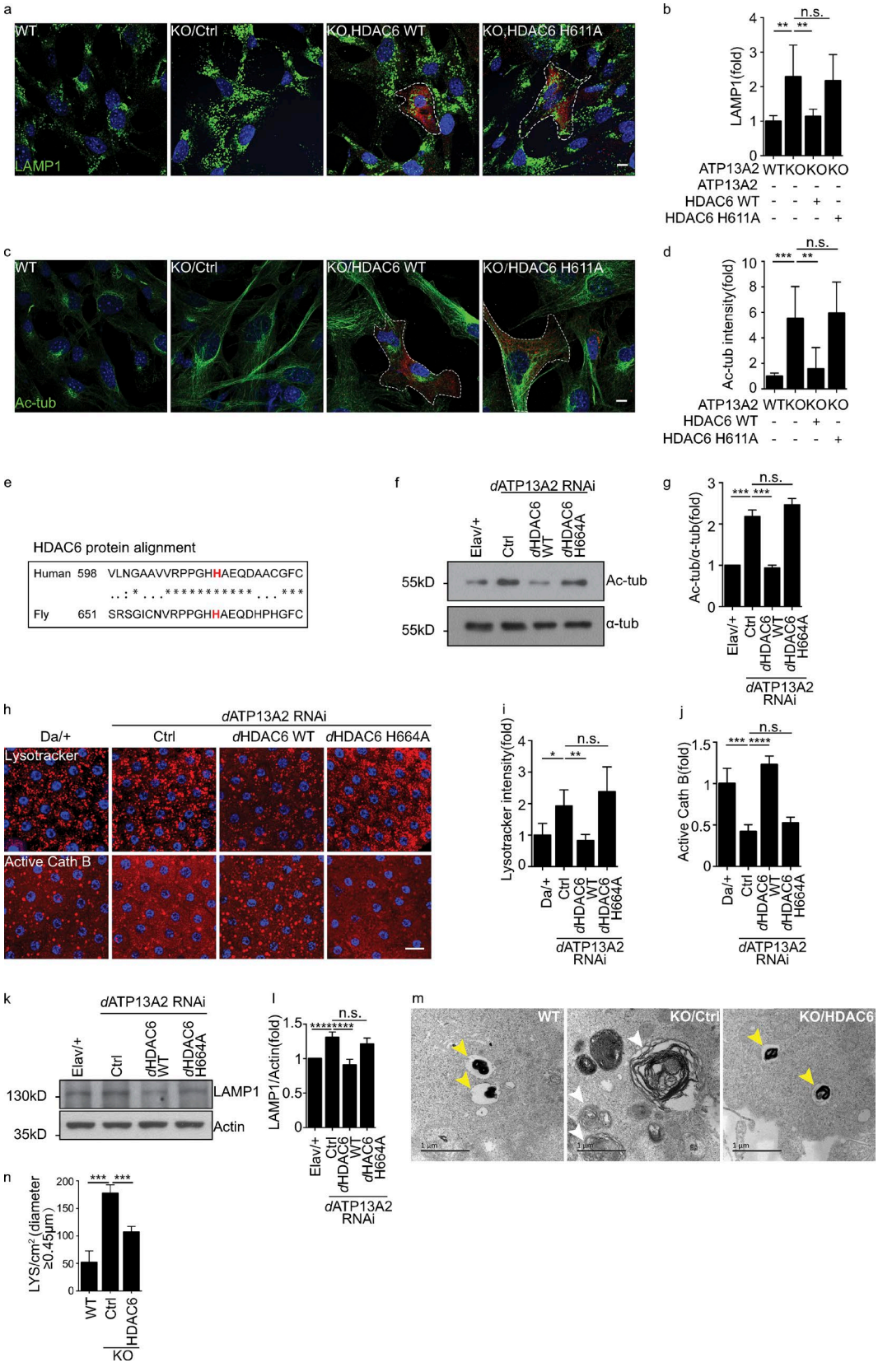

Figure 4. **HDAC6-dependent LYS accumulation with ATP13A2 deficiency. (a and b**) HDAC6 reverses LYS accumulation in ATP13A2-null MEFs. LYS in ATP13A2-null (KO/Ctrl) and control MEF cells (WT) were immunodetected for LAMP1 (green). Expression of HDAC6 (KO/HDAC6 WT), but not H664A mutant (KO/HDAC6 H664A), inhibited LYS accumulation in ATP13A2-null cells. Quantification of LAMP1-positive structures by ImageJ is shown (b). Bar, 10 µm. **, $P < 0.01$. WT: $n = 36$, KO: $n = 41$, KO/HDAC6 WT: $n = 39$, KO/HDAC6 H664A: $n = 46$. **(c and d)** ATP13A2-regulated α-tubulin acetylation is HDAC6 dependent. α-Tubulin acetylation (Ac-tub, green) was detected in WT MEFs (WT), ATP13A2-null MEFs (KO/Ctrl), ATP13A2-null MEFs expressing HDAC6 (KO/HDAC6 WT),

cin abolished fusion when both APS and LYS were isolated from WT mice (Fig. 5, k and l). Consistently, ATP13A2 did not affect APS–LYS tethering (Fig. 5, f–l) and recruitment of fusion regulatory protein Qa-SNARE STX17 to APS (Fig. S4 e). These findings suggest that ATP13A2 on LYS, but not on APS, promotes fusion.

LC3-II accumulation in ATP13A2-null HEK293 cells was rescued by HDAC6 overexpression (Fig. 5, m and n). Nevertheless, LC3-II levels in ATP13A2-null cells were comparable to those in WT control cells when APS–LYS fusion was inhibited by bafilomycin A1 (Fig. 5, m and n). Consistently, LC3 puncta in ATP13A2-null MEFs was markedly increased compared with that of control cells. Most fluorescent vesicles were red in control WT MEFs expressing GFP-mCherry-LC3. Nonfusing, yellow fluorescent vesicles were <40% (n = 178). By contrast, ATP13A2-null MEFs expressing GFP-mCherry-LC3 exhibited mostly nonfusing yellow fluorescent vesicles (>65%, n = 165). Expression of HDAC6 significantly reduced the number of yellow vesicles (<20%, n = 186) in ATP13A2-null MEFs (Fig. 5, o and p). Importantly, LC3 puncta were effectively cleared by expressing HDAC6, but not by HDAC6 H611A mutant (Fig. S4, f and g). Results further verify that ATP13A2 regulates APS–LYS fusion via an HDAC6-mediated mechanism. Loss of ATP13A2 leads to accumulation of both APS and LYS.

ATP13A2 recruits HDAC6 to LYS to facilitate cortactin acetylation

To identify the downstream target of the ATP13A2/HDAC6 pathway, we examined acetylation of cortactin, a protein implicated in APS–LYS fusion (Lee et al., 2010). In HEK293 cells overexpressing cortactin, levels of acetylated cortactin were increased in ATP13A2-null cells relative to control cells, supporting that HDAC6 activity was decreased in these cells (Fig. 6, a and b). The endogenous cortactin levels were similar in ATP13A2-null and control HEK293 cells, suggesting that ATP13A2 did not alter cortactin expression (Fig. 6, c and d). Remarkably, APS–LYS fusion was restored by overexpressing cortactin in ATP13A2-null MEFs (Fig. 6, e and f). Consistently, cortactin was less colocalized with lysosomal LAMP1 in ATP13A2-null MEFs compared with control MEFs (Fig. 6, g and h). Overexpression of HDAC6, but not the HDAC6 H611A mutant, facilitates cortactin localization to LYS in ATP13A2-null MEFs (Fig. 6, g and h). Fractionation analysis showed that HDAC6, cortactin, and actin in LYS of ATP13A2-null cells were significantly less compared with control cells (Fig. 6, i–l). HADC6 showed remarkable colocalization with LAMP1 in WT, but not in ATP13A2-null, HEK293 cells (Fig. 6 m). Furthermore, HADC6 activity is significantly higher in the lysosomal fraction isolated from WT mouse livers than that isolated from ATP13A2-null mouse livers. In contrast, HDAC6 activity remained the same in mitochondrial fractions isolated from livers of both WT and ATP13A2-null mice. HDAC6 inhibitor trichostatin A effectively inhibited HDAC6 activity in the lysosomal fraction isolated from WT mouse livers, demonstrating the specificity of HDAC6 activity assay (Fig. 6 n). The HDAC6 activity in cytosol fractions of livers isolated from both WT and ATP13A2-null mice were similar, but notably higher in LYS fractions isolated from WT mouse livers than from ATP13A2-null mouse livers. Furthermore, LYS addition to the assays showed little effect on HDAC6 activity of cytosol, suggesting that ATP13A2 likely recruits HDAC6 to LYS (Fig. S5 a). Together, ATP13A2 facilitates HDAC6 recruitment, therefore, of cortactin to LYS, leading to cortactin deacetylation and actin polymerization, to promote APS–LYS fusion and completion of autophagy.

The ATP13A2/HDAC6 pathway promotes clearance of insoluble proteins and damaged mitochondria

We next examined potential function of the ATP13A2/HDAC6 pathway on degradation of insoluble proteins and damaged mitochondria via autophagy. Treatment of both ATP13A2-null and control MEFs with the proteasome inhibitor MG132 resulted in formation and accumulation of ubiquitin-positive protein aggregates. Aggregated proteins were mostly degraded in control WT MEFs 18 h after MG132 removal (Fig. 7 a, upper panel). By contrast, substantial aggregates remained detectable in ATP13A2-null MEFs under the same conditions (Fig. 7 a, lower panel). Overexpression of HDAC6, but not HDAC6 H611A mutant, effectively promoted clearance of MG132-induced protein aggregates in ATP13A2-null MEFs (Fig. 7 b). Consistently, *dATP13A2* knockdown in *Drosophila* promoted formation of inclusion body–like protein aggregates in brain of 3-d-old flies. Inclusion bodies grew larger in 30-d-old flies. Remarkably, aggregate formation in *dATP13A2* knockdown fly brains was effectively suppressed by overexpressing *d*HDAC6 but not the *d*HDAC6 H664A mutant (Fig. 7, c and d). Likewise, levels of Triton X-100–insoluble ubiquitinated proteins increased in brains of

and ATP13A2-null MEFs expressing HDAC6 H611A (KO/HDAC6 H611A). HDAC6 variants were detected with an anti-FLAG antibody (red). Cell boundary was labeled by dashed lines. Bar, 5 µm (c and e). Quantification of Ac-tub intensity per cell was done with ImageJ. **, P < 0.01; ***, P < 0.001. WT: n = 41, KO: n = 38, KO/HDAC6 WT: n = 31, KO/HDAC6 H611A: n = 46. **(e)** Alignment of human and *Drosophila* HDAC6 (Fly) catalytic domain. Red indicates the active histidine (H). **(f and g)** *d*HDAC6 reduces tubulin acetylation in *d*ATP13A2 RNAi fly. Fly brain lysates were immunodetected for acetylated tubulin (Ac-tub) and total tubulin (α-tub). WT fly expressing elav-gal4 alone (Elav/+) and *d*ATP13A2 RNAi fly (RNAi) expressing elav-gal4 alone (Ctrl), *d*HDAC6 (*d*HDAC6 WT), or *d*HDAC6 H664A mutant (*d*HDAC6 H664A) were analyzed (d). Quantitative analysis is shown (e). ***, P < 0.001, n = 3. **(h–j)** *d*ATP13A2 RNAi caused *d*HDAC6 dependent LYS accumulation. Fly follicle cells were probed with LysoTracker (upper panel) and active cathepsin B (Active Cath B, lower panel). Control Da-gal4 expressor (Da/+) and *dATP13A2* RNAi line (RNAi) expressing Da-gal4 alone (Ctrl), *d*HDAC6 (*d*HDAC6 WT), or *d*HDAC6 H664A mutant (*d*HDAC6 H664A) (f). Quantitative analysis of LysoTracker intensity (g) and active cathepsin B (h) are shown. Bar, 10 µm. *, P < 0.05; **, P < 0.01; ***, P < 0.001; ****, P < 0.0001. For Lysotracker: Da/+: n = 7, Ctrl: n = 6, *d*HDAC6 WT: n = 7, *d*HDAC6 H664A: n = 9. For active CathB: Da/+: n = 7, Ctrl: n = 6, *d*HDAC6 WT: n = 7, *d*HDAC6 H664A: n = 6. **(k and l)** *d*ATP13A2 RNAi causes *d*HDAC6-dependent LAMP1 increase. Fly head lysates were immunodetected for LAMP1 and actin. The control elav-gal4 expressor (Elav/+) and *dATP13A2* RNAi line (RNAi) expressing either elav-gal4 alone (Ctrl), WT *d*HDAC6 (*d*HDAC6 WT), or *d*HDAC6 H664A (*d*HDAC6 H664A) were analyzed (i). Quantitative analysis is shown (j; n = 3). ***, P < 0.001; ****, P < 0.0001. **(m and n)** TEM analysis of LYS. WT, ATP13A2-null HEK293 cells (KO/Ctrl) and their HDAC6 expressors (KO/HDAC6) were starved and analyzed by TEM. Normal LYS (yellow arrowheads) and abnormal LYS (white arrowheads) are indicated. Bar, 1 µm. Quantitation of large LYS (diameter, >0.45 µm) is shown (n). ***, P < 0.001. WT: n = 21, KO/Ctrl: n = 32, KO/HDAC6: n = 26.

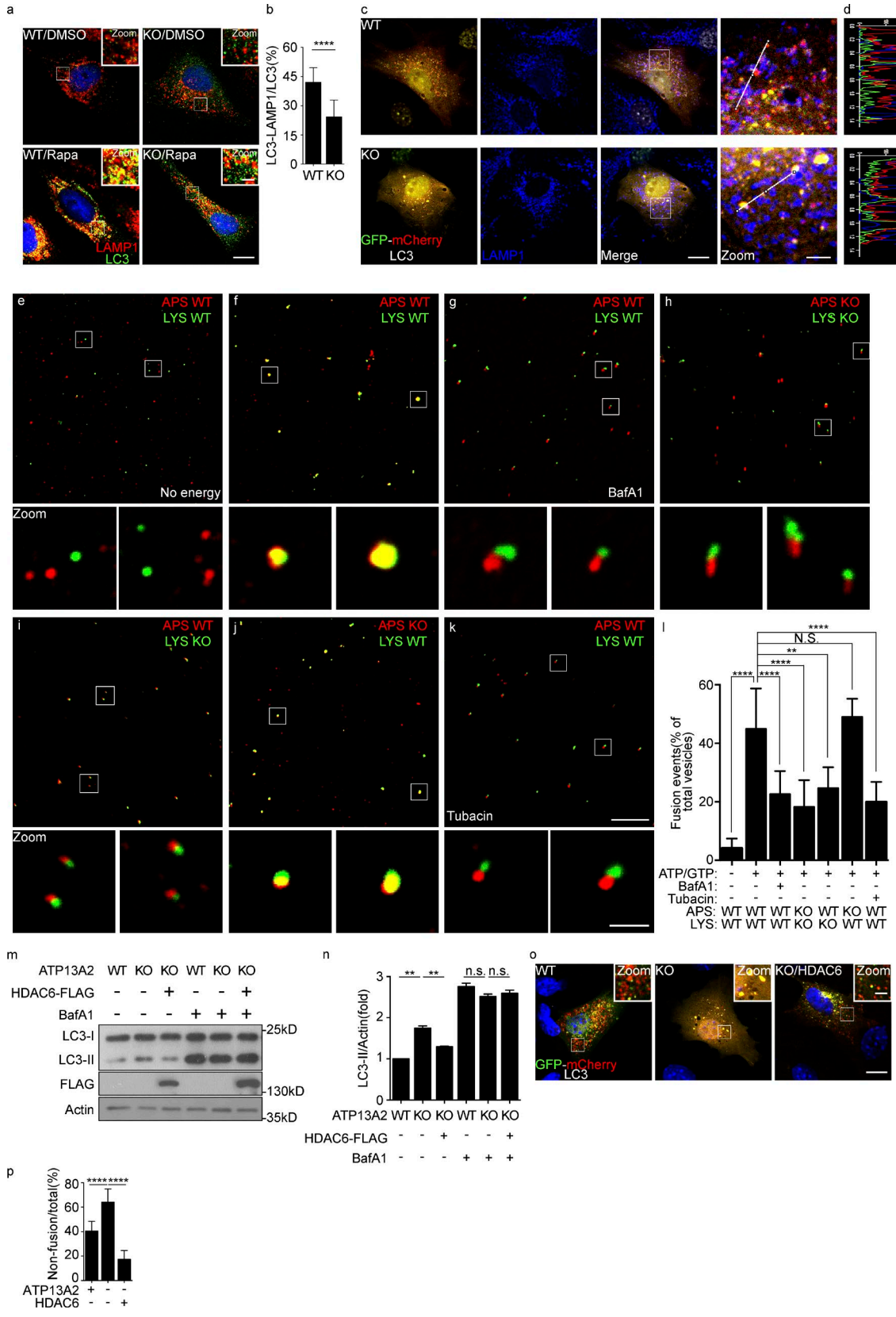

Figure 5. **ATP13A2 regulation of APS–LYS fusion is HDAC6 dependent. (a and b)** Reduced colocalization of endogenous LC3 and LAMP1 in ATP13A2-null HeLa cells. Control (WT) and ATP13A2-null (KO) HeLa cells were treated with DMSO (a, upper panels) or rapamycin for 16 h to induce autophagy (a, lower panels, Rapa). Immunodetection of endogenous LAMP1 (red) and LC3 (green) at lower (bar, 7.5 µm) and higher (insets; bar, 1.5 µm) magnification is shown (a). LC3-LAMP1 colocalization in the rapamycin-treated group is shown (b; WT/Rapa: $n = 48$, KO/Rapa: $n = 59$). ****, $P < 0.0001$. **(c and d)** Colocalization of GFP-mCherry-LC3 and LAMP1. Control (WT) and ATP13A2-null (KO) MEFs expressing GFP-mCherry-LC3 were immunodetected for LAMP1 (blue). Colocalization

dATP13A2 knockdown flies relative to WT controls. The increase was reversed by overexpressing *d*HDAC6 but not *d*HDAC6 H664A mutant. Levels of Triton X-100–soluble ubiquitinated proteins were comparable in control and *d*ATP13A2-knockdown flies (Fig. 7, e and f). Insoluble proteins were markedly increased in brains of flies fed with HDAC6 inhibitor tubastatin A for 30 d (data not shown). Consistently, climbing ability was significantly decreased in *d*ATP13A2 RNAi flies compared with WT control flies. The decreased motility was largely rescued by overexpressing *d*HDAC6, but not by *d*HDAC6 H664A mutant (Fig. S5 b). These results suggest that ATP13A2 promotes degradation of insoluble proteins by maintaining HDAC6 activity in both cultured cells and *Drosophila* neurons.

In parallel, we found that control HEK293 cells treated with the mitochondrial uncoupler cyanide m-chlorophenylhydrazone (CCCP) showed increased mitophagy and decreased mitochondrial DNA (mtDNA) content compared with those treated with control solvent. By contrast, mtDNA content was only slightly reduced by CCCP treatment in ATP13A2-null cells. Overexpression of HDAC6 promoted CCCP-induced mitochondrial clearance (Fig. 7 g). Consistently, CCCP treatment induced reduction of mitochondrial inner membrane protein TIM23 in HEK293 cells, but not in ATP13A2-null HEK293 cells (Fig. S5, c and d), suggesting mitophagy impairment in cells lacking ATP13A2. TEM analysis revealed an increase of large APS containing damaged mitochondria in CCCP-treated ATP13A2-null HEK293 cells compared with controls (Fig. 7 h). These results suggest that ATP13A2 also facilitates clearance of damaged mitochondria via an HDAC6-mediated mechanism.

KRS pathogenic mutants are impaired in facilitating APS–LYS fusion and protein aggregate clearance

To analyze ATP13A2-regulated APS–LYS fusion in a disease context, we coexpressed GFP-mCherry-LC3 with one of the three KRS pathogenic ATP13A2 mutants, including one with a C-terminal 117–amino acid deletion (delC) and two point mutants (F182L and G504R), in ATP13A2-null MEFs (Ramirez et al., 2006; Tan et al., 2011). MEFs expressing WT ATP13A2 displayed primarily red fluorescent LC3-positive vesicles, indicating completion of fusion. By contrast, MEFs expressing any of the three mutants were primarily unfused with yellow fluorescence of LC3-positive vesicles (Fig. 8, a and b). Consistently, LC3 vesicles were accumulated in ATP13A2-null HeLa cells expressing pathogenic mutants (Fig. 8, c and d). Immunoblotting revealed increased α-tubulin acetylation and LC3-II accumulation in ATP13A2-null HEK293 cells more than those in their WT control cells. Expression of ATP13A2, but not the delC, F182L, and G504R mutants, suppressed α-tubulin acetylation and LC3-II accumulation in ATP13A2-null HEK293 cells (Fig. 8, e–g). All three mutants were degraded rapidly under normal culture conditions via ubiquitin proteasome system (Fig. 8 e and data not shown). Furthermore, MG132-induced ubiquitin-positive insoluble proteins seen in ATP13A2-null MEF cells did not undergo degradation in cells expressing any of the three mutants, whereas the insoluble proteins were effectively degraded in cells expressing WT ATP13A2 (Fig. 8 h). These results suggest that disease-associated mutants are impaired in facilitating APS–LYS fusion and clearance of abnormal proteins and damaged cell organelles.

Discussion

The major finding of this study is the identification of ATP13A2 as an essential molecule for maintaining normal autophagy via regulating HDAC6 lysosomal localization and activity to control APS–LYS fusion. Impaired ATP13A2/HDAC6 signaling likely contributes to KRS and PD pathogenesis by disrupting clearance of protein aggregates and damaged mitochondria, further defining the molecular insights underlying these diseases. Our results suggest a potential therapeutic strategy in these conditions of targeting HDAC6 to increase its activity in brain.

Autophagy degrades protein aggregates and damaged organelles to provide nutrients and energy for cellular repair and homeostasis, which requires APS formation and APS–LYS fusion (Levine and Kroemer, 2008; Bento et al., 2016b). In this study, we first show ablation of ATP13A2 results in aging-dependent impairment of autophagy in vivo. We demonstrate that ATP13A2 recruits HDAC6 to LYS to control APS–LYS fusion. Four lines of evidence support that ATP13A2 facilitates HDAC6 activity. First, ATP13A2 inactivation promotes marked hyperacetylation of α-tubulin and cortactin. Second, HDAC6 activity is significantly lower in ATP13A2-null cells than in control cells, indicating reduced HDAC6 deacetylation activity in ATP13A2-null cells. Third, WT HDAC6, but not the deacetylase catalytic mutant, rescues multiple abnormalities caused by ATP13A2 deficiency, suggesting the importance of HDAC6 deacetylase activity. Last, loss of ATP13A2 causes HDAC6-dependent accumulation of both APS and LYS. Thus, ATP13A2 is essential for normal HDAC6 activity in vitro and in vivo. ATP13A2/HDAC6 signaling likely

of GFP-mCherry-LC3 and LAMP1 is shown at low (merged image; bar, 7.5 µm) and high (zoom; bar, 1.5 µm) magnification (c). Representative histograms of colocalization are shown (d). Red–blue colocalization is seen in control MEFs; green–red colocalization is detected in ATP13A2-null MEFs (d). **(e–l)** In vitro reconstitution of APS–LYS fusion. APS and LYS were isolated from livers of starved ATP13A2-null (KO) mice or their control littermates (WT). APS (red) and LYS (green) were labeled with an anti-LC3B antibody and an anti-LAMP1 antibody, respectively. Fusion was assessed in energy-regenerating buffer supplied with various APS and LYS combinations. Fusion of both APS and LYS from WT mouse livers in the absence of ATP/GTP/creatine phosphokinase (e; No energy) or with (g; BafA1) or without (f) the fusion inhibitor bafilomycin A1 served as controls. Results of other indicated combinations are shown in h, i, and j. HDAC6 inhibitor tubacin was also included to show essential roles of HDAC6 in APS–LYS fusion (k). Bar, 7.5 µm; Zoom, bar, 1.5 µm. Quantitative analysis of fused versus total vesicles is shown (j). **, $P < 0.01$; ****, $P < 0.0001$, $n = 4$. **(m and n)** HDAC6 reverses LC3 accumulation in ATP13A2-null cells. Control (WT) and ATP13A2-null (KO) HEK293 cells expressing control plasmid (HDAC6-FLAG, –) or HDAC6-flag (HDAC6-FLAG, +) followed by treatment with DMSO (BafA1, –) or bafilomycin A1 (BafA1, +). LC3 (both LC3-I and LC3-II), HDAC6 (FLAG), and actin were immunodetected (m). Quantitative analysis is shown (n). **, $P < 0.01$, $n = 3$. **(o and p)** HDAC6 rescues ATP13A2-null impaired fusion. WT MEFs (WT) and ATP13A2-null MEFs (KO) cotransfected GFP-mCherry-LC3 reporter with either pcDNA3.1 (KO) or WT HDAC6 (HDAC6) were imaged for fusion. Both lower (bar, 7.5 µm) and higher (o; Zoom, bar, 1.5 µm) magnification images are shown. Analysis of nonfused (yellow) versus total vesicles is shown (p). ****, $P < 0.0001$. WT: $n = 178$, KO: $n = 165$, KO/HDAC6: $n = 186$.

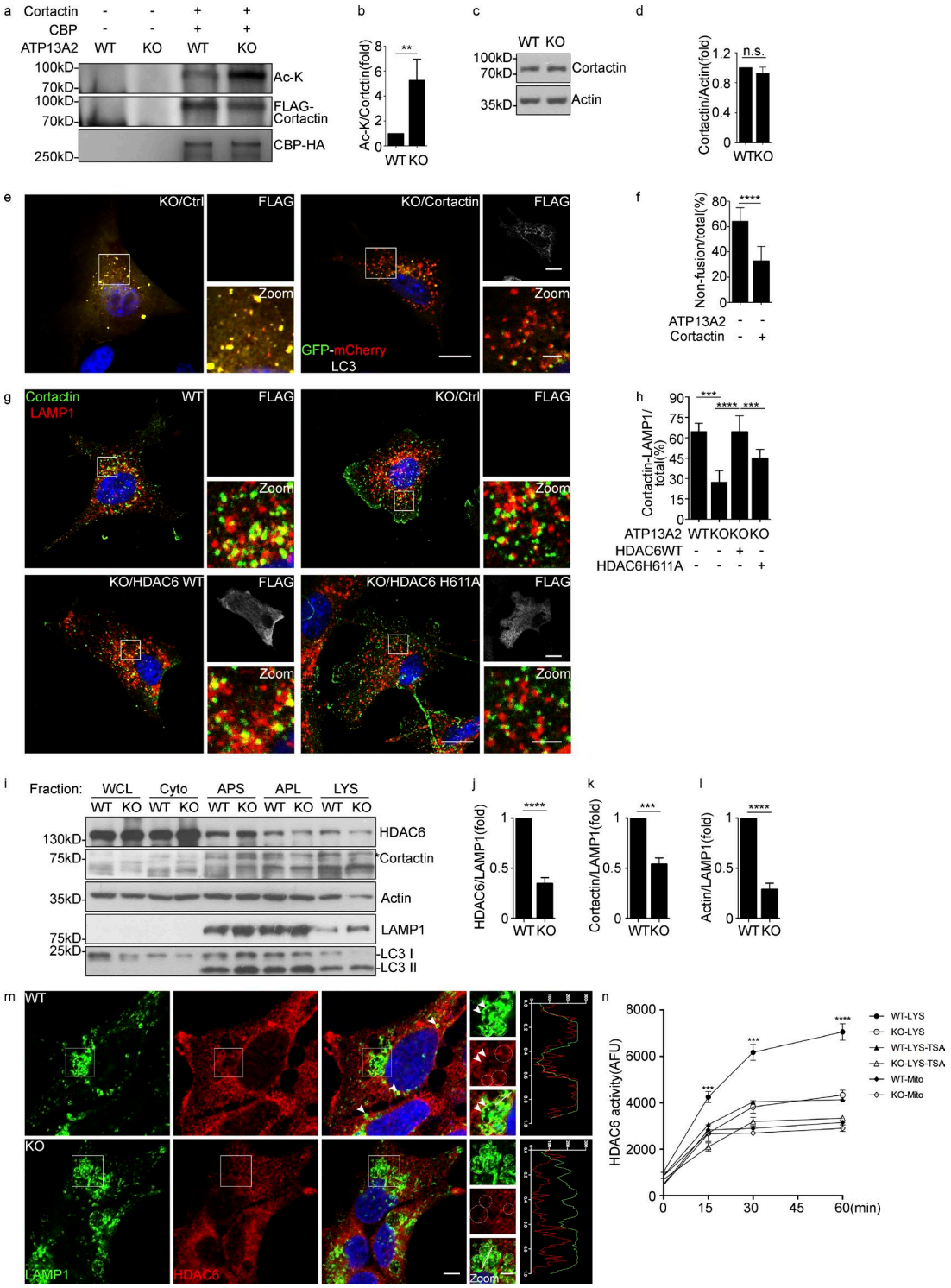

Figure 6. **ATP13A2 regulates cortactin acetylation to promote APS–LYS fusion. (a and b)** ATP13A2 regulates cortactin acetylation. Control (ATP13A2, WT) and ATP13A2-null (ATP13A2, KO) HEK293 cells were cotransfected with CBP (CBP, +) and either control empty plasmid (Cortactin, –) or a plasmid encoding FLAG-cortactin (Cortactin, +). Cortactin was immunoprecipitated followed by immunoblot analysis with an anti-acetylated lysine (Ac-K), an anti-FLAG-tag (FLAG-Cortactin), or anti-CBP antibodies (CBP; a). Relative levels of acetylated cortactin are shown (b). **, $P < 0.01$, $n = 3$. **(c and d)** Endogenous cortactin levels are not affected in ATP13A2. Expression of endogenous cortactin and actin in ATP13A2-null (KO) and WT control (WT) MEFs was detected (c). Quantitative analysis is shown (d; $n = 3$). **(e and f)** Cortactin rescues APS–LYS fusion in ATP13A2-null MEFs. ATP13A2-null MEFs (KO) were cotransfected with a plasmid encoding GFP-mCherry-LC3 with either an empty pCMV plasmid (KO/Ctrl) or a plasmid encoding FLAG-cortactin (KO/Cortactin). Fusion (red), nonfusion (yellow), exogenous cortactin (FLAG, white; bar, 7.5 µm), and high-magnification images (Zoom, bar, 1.5 µm) are shown (e). Quantitation of nonfused over total vesicles is shown (f). ****, $P < 0.0001$. KO/Ctrl: $n = 37$, KO/Cortactin: $n = 46$. **(g and h)** ATP13A2 and HDAC6 regulate cortactin/LYS colocalization. WT or ATP13A2-null (KO) MEFs transfected with control plasmid pcDNA3.1 (Ctrl), a plasmid encoding HDAC6 (HDAC6 WT), or a plasmid encoding HDAC6 mutant (HDAC6 H611A) were immunodetected for cortactin (green) and LAMP1 (red). Bar, 7.5 µm. Exogenous HDAC6 (FLAG, white; bar, 7.5 µm) and higher -magnification images (Zoom, bar,

constitutes a common mechanism for regulating APS–LYS fusion in autophagy. We have noted that phenotypes of ATP13A2-null mice are milder than those of autophagy-associated factor–null mice. It is possible that ATP13A2 function is compensated by other P-type ATPases during development and in young age. The compensatory mechanism is impaired with aging. Therefore, the mouse develops abnormalities that potentially contribute to aging-dependent neurodegeneration.

HDAC6 regulates selective autophagy, at least partially, by promoting APS–LYS fusion (Lee et al., 2010). Consistently, ATP13A2 deficiency perturbs fusion of APS and LYS in cells and in in vitro reconstitution assays. LC3-II accumulation in ATP13A2-null cells further suggests that the autophagic degradation process is compromised in these cells. Importantly, impaired fusion caused by ATP13A2 deficiency can be restored by overexpressing HDAC6, demonstrating the critical role of HDAC6 in ATP13A2-mediated fusion. How ATP13A2 facilitates HDAC6 activity remains unclear. One potential mechanism is that ATP13A2 facilitates recruitment of HDAC6 to LYS to increase its local concentration and activity, enabling cortactin deacetylation and leading to local assembly of a microfilament network that favors APS–LYS fusion and eventual autophagic degradation. Accordingly, we find that ATP13A2 interacts with HDAC6. ATP13A2 on LYS, but not on APS, is essential for APS–LYS fusion. More HDAC6, cortactin, and actin are detected in the lysosomal fraction in WT control cells than in ATP13A2-null cells. Cortactin acetylation changes assembly of both F-actin and microtubules to modulate autophagy, particularly in activities related to APS–LYS fusion (Zhang et al., 2007; Lee et al., 2010; Bánréti et al., 2013). Our results demonstrate that cortactin deacetylation and translocation to LYS is ATP13A2 dependent. In ATP13A2-null cells, cortactin is highly acetylated, and its recruitment to LYS is impaired. Notably, overexpression of either HDAC6 or cortactin promotes APS–LYS fusion in ATP13A2-null cells. ATP13A2 may also regulate HDAC6 activity by maintaining proper zinc concentration, as ATP13A2 reportedly maintains physiological concentrations of zinc ion (Kong et al., 2014; Park et al., 2014; Tsunemi and Krainc, 2014). Zinc is essential to sustain HDAC6 function and conformation (Boyault et al., 2006; Hao et al., 2013).

ATP13A2 plays an important role in maintaining LYS homeostasis. Lysosomal structure and function become abnormal in neurons of ATP13A2-null mouse brains (Dehay et al., 2012; Kett et al., 2015; Bento et al., 2016a). Consistently, we have found abnormal structures and reduced lysosomal hydrolase activity in ATP13A2-deficient cells and brain tissues of *Drosophila* and mouse. Importantly, lysosomal abnormalities caused by ATP13A2 inactivation are rescued by HDAC6 expression, indicating that LYS itself is not impaired by lacking ATP13A2; instead, that the ATP13A2/HDAC6 pathway likely functions in maintaining maturation and recycling of LYS. One potential mechanism is that the ATP13A2/HDAC6 pathway promotes autophagy, leading to increased generation and recycling of LYS. Inactivation of ATP13A2/HDAC6 results in accumulation of aged LYS. A recent study shows that ATP13A2 regulates SYT11, a protein functioning in calcium-dependent vesicular fusion and trafficking, at both transcriptional and posttranslational levels, suggesting that this regulation may alter either APS–LYS fusion or lysosomal activity (Bento et al., 2016a). Whether SYT11 functions in HDAC6-mediated fusion remains unclear. Abnormalities in transcription of lysosomal proteins in ATP13A2-null cells may be caused by negative feedback associated with LYS accumulation. Mechanisms underlying these effects warrant further investigation.

Our results suggest that impaired APS–LYS fusion is a potential pathogenic mechanism underlying ATP13A2 disease mutants. ATP13A2 mutants inhibit autophagic degradation, leading to accumulation of insoluble proteins and damaged mitochondria in vitro and in vivo. This finding may explain why ubiquitinated protein aggregates, lipofuscinosis, and endolysosomal abnormalities are often observed in ATP13A2-null mouse models (Usenovic et al., 2012b; Schultheis et al., 2013; Park et al., 2014; Kett et al., 2015; Sato et al., 2016). Lewy body formation and mitochondrial dysfunction are PD hallmarks. KRS-associated mutants in particular fail to rescue several phenotypes seen in ATP13A2-null cells, among them, impaired APS–LYS fusion, reduced autophagic flux, or failure to degrade aggregated proteins, supporting a potential role of ATP13A2 loss in KRS or PD pathogenesis. This study opens a new avenue to design treatment strategies to target HDAC6-mediated autophagy for these diseases.

Materials and methods

Plasmids, antibodies, and chemicals

Human HDAC6-FLAG (30482), GFP-CTTN (50728), pLAMP1-mCherry (45147), and pH-sensitive GFP-mCherry-LC3 (22418) plasmids were purchased from Addgene. ATP13A2 WT and pathogenic delC mutant were from Christian Kubisch (Institute of Human Genetics, University of Cologne, Cologne, Germany; Tan et al., 2011). The HDAC6 deacetylation-inactive mutant H611A and ATP13A2 F182L and G504R mutants were generated with a QuikChange site-directed Mutagenesis Kit from Stratagene according to the manufacturer's instructions. cDNA encod-

1.5 µm) are also shown. Quantitative analysis of LAMP1-cortactin colocalization is shown (h). ***, P < 0.001; ****, P < 0.0001. WT: *n* = 39, KO/Ctrl: *n* = 41, KO/HDAC6 WT: *n* = 33, KO/HDAC6 H611A: *n* = 47. **(i–l)** Fractionation analysis of HDAC6 and cortactin in mouse liver tissues. Livers of ATP13A2-null mice (KO) and their WT control littermates (WT) were fractionated to isolate cytoplasm (Cyto), APS, autophagolysosome (APL), and LYS. The lysates of fractions and whole-cell lysates (WCL) were immunodetected for HDAC6, cortactin, actin, LAMP1, or LC3 (i). *, cortactin. The relative levels of HDAC6 (j), cortactin (k), and actin (l) in the lysosomal fraction of ATP13A2-null (KO) and their WT controls were calculated. ***, P < 0.001; ****, P < 0.0001, *n* = 3. **(m)** ATP13A2 regulates HDAC6 lysosomal localization. WT and ATP13A2-null (KO) HEK293 cells were immunodetected for LAMP1 (green) and HDAC6 (red). Bar, 5 µm. Arrows and dotted-line circles indicate LYS and HDAC6. The solid line in higher magnification images (Zoom; bar, 2.5 µm) indicates where colocalization analysis was performed. Histograms of LAMP1 and HDAC6 colocalization are shown (right panel). Bar, 5 µm. **(n)** Lysosomal HDAC6 activity is regulated by ATP13A2. HDAC6 activity of LYS and mitochondria (Mito) isolated from livers of WT or ATP13A2-null mice were assayed at 0, 15, 30, and 60 min. LYS fractions treated with trichostatin A were analyzed as a negative control. ***, P < 0.001; ****, P < 0.0001, *n* = 3.

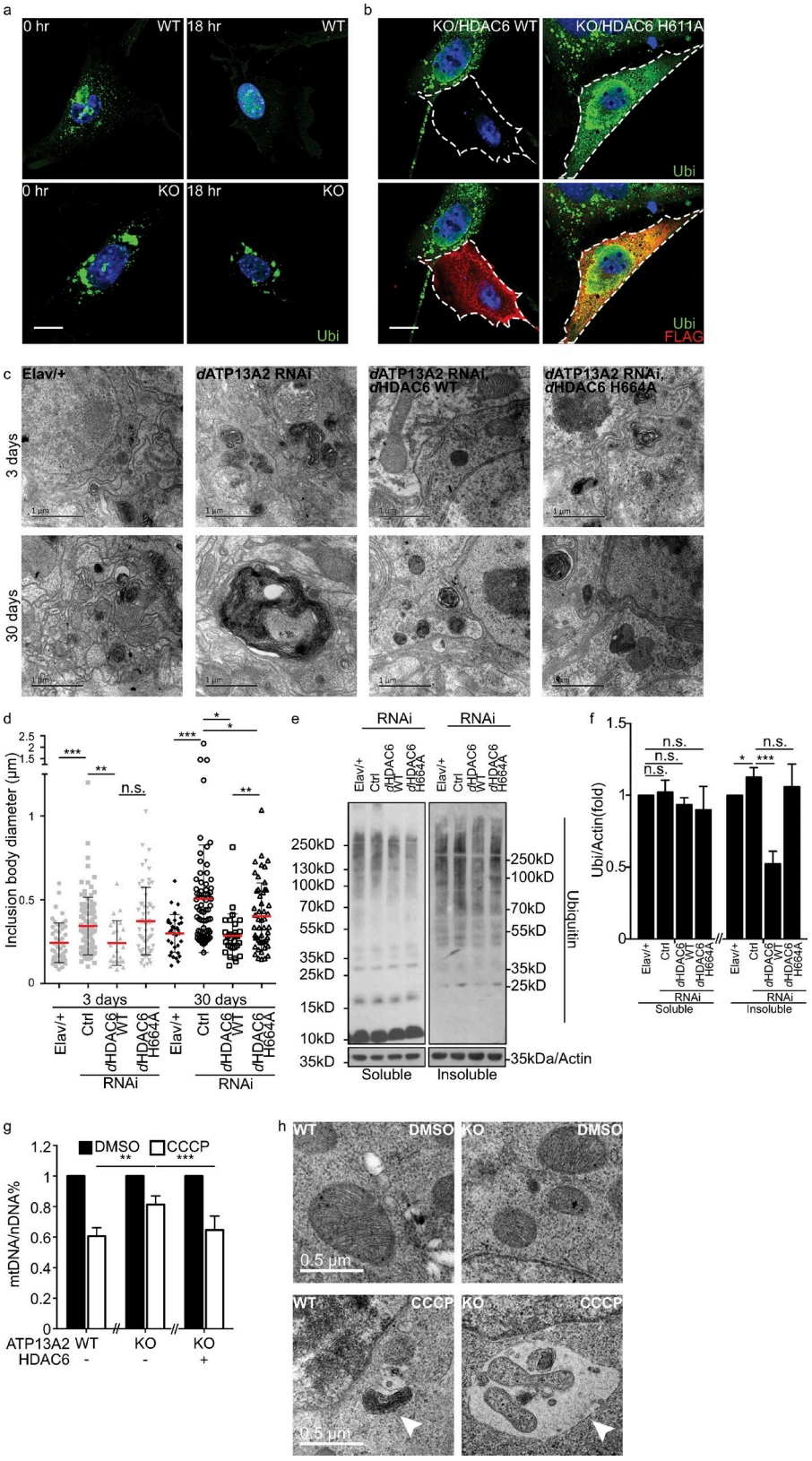

Figure 7. **Impaired degradation of protein aggregates and damaged mitochondria in ATP13A2-null MEFs and *d*ATP13A2 RNAi fly brains. (a)** Impaired degradation of protein aggregates in ATP13A2-null cells. Control (WT, upper panel) and ATP13A2-null MEFs (KO, lower panel) were treated with MG132 for 12 h to induce protein aggregation followed by MG132 removal for 0 or 18 h. Protein aggregates were detected with an anti-ubiquitin antibody (Ubi, green). Nuclei were DAPI-stained (blue). Bar, 7.5 μm. **(b)** HDAC6 expression rescues impaired aggregate degradation. ATP13A2-null MEFs (KO) were transfected with HDAC6 (WT) or the HDAC6 H611A mutant. Cells were treated with MG132 for 12 h to induce protein aggregation followed by MG132 removal for 18 h. Protein aggregates (Ubi, green) and exogenous HDAC6 (FLAG, red; lower panel) were detected. Nuclei were DAPI-stained (blue). Dashed lines indicate transfectant of HDAC6 variants. Bar, 7.5 μm. **(c and d)** TEM analysis of fly brain. Brains were dissected from 3-d-old (c, upper panel) and 30-d-old (c, lower panel) flies followed by TEM analysis. Control flies expressing elav-gal4 only (Elav/+), flies expressing *d*ATP13A2 RNAi (*d*ATP13A2 RNAi), flies expressing both *d*ATP13A2 RNAi and WT *d*HDAC6 (*d*ATP13A2 RNAi, *d*HDAC6 WT), or flies expressing both *d*ATP13A2 RNAi and *d*HDAC6 H664A mutant (*d*ATP13A2 RNAi, *d*HDAC6 H664A) were analyzed. Bar, 1 μm. Quantitation of inclusion body diameter is shown (d). *, $P < 0.05$; **, $P < 0.005$; ***, $P < 0.001$. For 3 d, Elav/+: $n = 51$, *d*ATP13A2 RNAi: $n = 103$, *d*ATP13A2 RNAi/*d*HDAC6 WT: $n = 48$, *d*ATP13A2 RNAi/*d*HDAC6 H664A: $n = 63$. For 30 d: Elav/+: $n = 33$, *d*ATP13A2 RNAi: $n = 70$, *d*ATP13A2 RNAi/*d*HDAC6 WT: $n = 31$, *d*ATP13A2 RNAi/*d*HDAC6 H664A: $n = 51$. **(e and f)** Accumulation of insoluble proteins in *d*ATP13A2-RNAi fly brains. Triton X-100–soluble (left panel) and –insoluble (right panel) proteins were extracted from *d*ATP13A2 RNAi fly brains. Ubiquitinated proteins (Ubi) and actin were detected (e). Control flies expressing elav-gal4 only (Elav/+), flies expressing *d*ATP13A2 RNAi (*d*ATP13A2 RNAi), flies expressing both *d*ATP13A2 RNAi and WT *d*HDAC6 (*d*ATP13A2 RNAi, *d*HDAC6 WT), or flies expressing both *d*ATP13A2 RNAi and *d*HDAC6 H664A mutant (*d*ATP13A2 RNAi, *d*HDAC6 H664A) were analyzed. Quantitative analysis is shown (f). *, $P < 0.05$; ***, $P < 0.001$, $n = 3$. **(g)** Impaired clearance of damaged mitochondria in ATP13A2-null HEK293 cells. Control (ATP13A2, WT) and ATP13A2-null (ATP13A2, KO) HEK293 cells transfected with either pcDNA3.1 (HDAC6, –) or HDAC6 (HDAC6, +) were treated with either DMSO (filled bar) or CCCP (empty bar) for 12 h. mtDNA/nDNA ratios were calculated. **, $P < 0.01$; ***, $P < 0.001$, $n = 3$. **(h)** TEM analysis of CCCP-induced mitophagy in ATP13A2-null HEK293 cells. Control and ATP13A2-null (KO) HEK293 cells were treated with either DMSO or CCCP followed by TEM analysis. Representative images of damaged mitochondria in APS (white arrows) are shown. Bar, 0.5 μm.

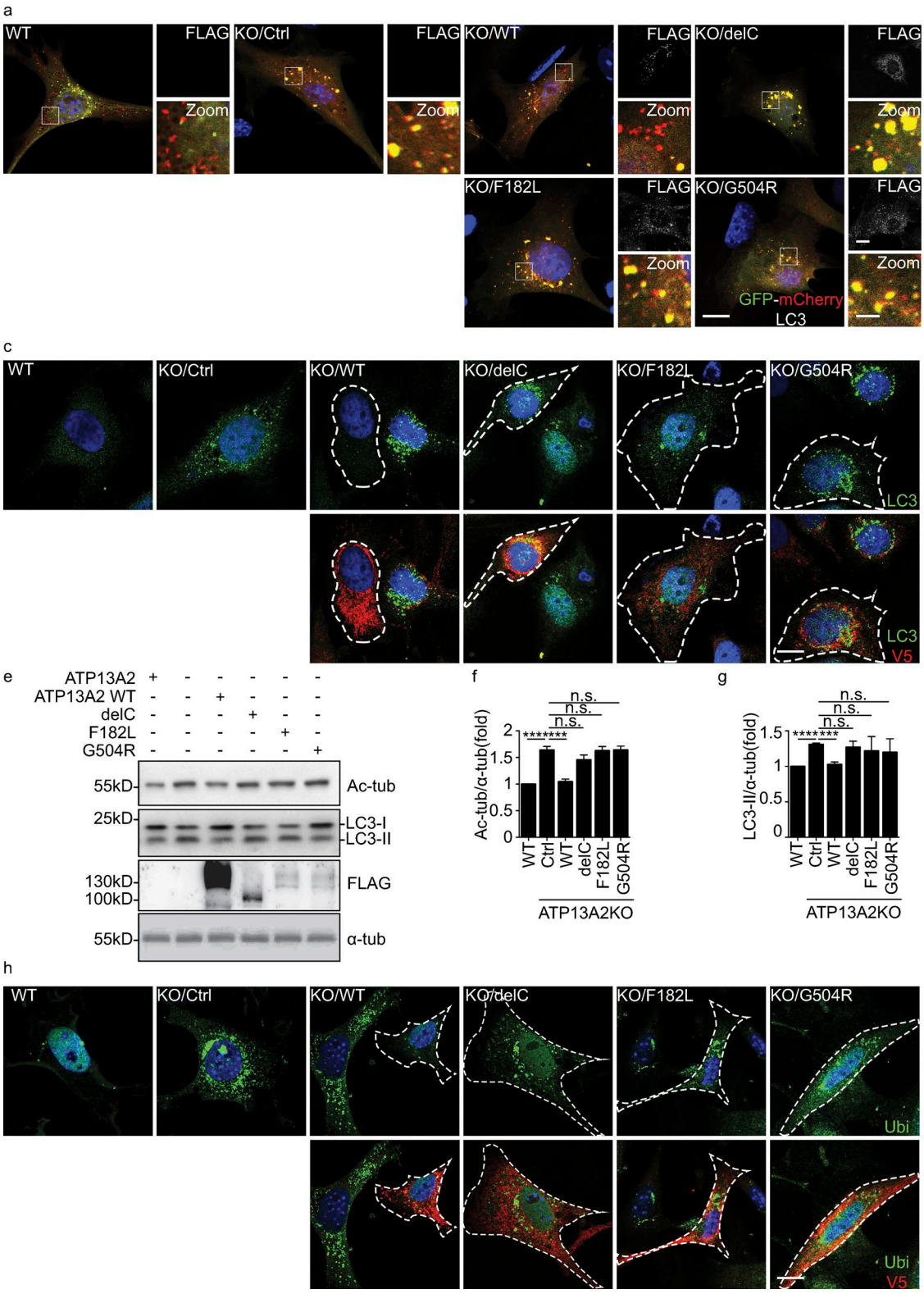

Figure 8. **KRS pathogenic ATP13A2 mutants fail to rescue defects of ATP13A2-null cells. (a and b)** ATP13A2 pathogenic mutants do not rescue APS–LYS fusion. WT or ATP13A2-null (ATP13A2 KO) MEFs expressing GFP-mCherry-LC3 plus a control (Ctrl), ATP13A2WT, delC, F182L, or G504R plasmid. Fusion (red) or nonfusion (yellow) of APS–LYS is shown (a). Bar, 7.5 µm. Insets: expression of ATP13A2 variants (FLAG, white; bar, 7.5 µm) and magnified images (Zoom, bar, 1.5 µm). Fusion events were quantitatively analyzed (b). ***, P < 0.001; ****, P < 0.0001, WT: *n* = 31, KO/Ctrl: *n* = 37, KO/WT: *n* = 41, KO/delC: *n* = 33, KO/F182L: *n* = 29, KO/G504R: *n* = 27. **(c and d)** LC3 vesicle accumulation in cells expressing ATP13A2 pathogenic mutants. ATP13A2-null (ATP13A2 KO) HeLa cells expressing ATP13A2 (WT), delC, F182L, or G504R were detected for LC3 (green, upper panels) or ATP13A2 variants (V5, red, lower panels). Control (WT) and ATP13A2-null HeLa cells transfected with an empty plasmid (KO/Ctrl) served as controls (c). Bar, 7.5 µm. Quantitative analysis of LC3 puncta is shown (d). ****, P < 0.0001, *n* = 3. **(e–g)** ATP13A2 pathogenic mutants do not restore tubulin acetylation and LC3-II degradation in ATP13A2-null cells. ATP13A2-null (ATP13A2

ing cortactin was subcloned into pCMV-3xFLAG with EcoRI and BamHI. cDNA encoding STX-17 was subcloned into pEGFP-C1 with HindIII and BamHI from New England Biolabs.

Anti-LAMP1 (sc18821, mouse), anti-LAMP2 (sc18822, mouse), and anti-LAMP1 (sc19992, rat) antibodies were from Santa Cruz Biotechnology. Antibodies for LC3B (2775s and 3868, both rabbit), HDAC6 (7558 and 7612, both rabbit), ubiquitin (3936, mouse), and FLAG-tag (14793, rabbit) were from Cell Signaling Technology. Anti-LC3 (PM036, rabbit) was from MBL. Anti-ubiquitin (BML-PW8810, mouse) was from Enzo Life Technology. Anti–α-tubulin (ab18251, rabbit) and anti-*Drosophila* LAMP1 (ab30687, rabbit) antibodies were from Abcam. Monoclonal antibodies against acetyl-α-tubulin (T7451, mouse), FLAG tags (M2, mouse), conjugated agarose (A2220), and p62/SQSTM1 (P0067, rabbit) were from Sigma-Aldrich. Anti-cortactin (05-180, mouse) was from Millipore. Anti-acetyl lysine (icp0380, rabbit) was from ImmunoChemistry Technologies.

Bafilomycin A1, tubacin, Tubastatin A, and MG132 were from Sigma-Aldrich. Tricostatin A and the phosphatase inhibitor cocktail were from Selleckchem. The protease inhibitor cocktail complete was from Roche. All other chemicals were from Sigma-Aldrich.

Cell lines, mice, and fly stocks

HEK293 and HeLa cells were obtained from ATCC and maintained as recommended by the provider. ATP13A2-null HEK293 and HeLa cells and HDAC6-null HEK293 cells were generated by the CRISPR-Cas9 system, as described (Sanjana et al., 2014; Shalem et al., 2014). In brief, the targeting sgRNA sequences (*ATP13A2*: 5′-CCAGTAGCCGATAGTGCAGC-3′; *HDAC6*: 5′-CGCGTAGAACGCCTAGTACA-3′) were subcloned into LentiCRISPR v2 (49535; Addgene). Recombinant LentiCRISPR plasmid was cotransfected with pCMV-VSV-G (8454; Addgene) and psPAX2 (12260; Addgene) into cells to package infectious lentivirus. Medium containing viruses was used to infect cells for 8 h, and cells were then selected in 0.5 µg/ml puromycin. Resistant clones were isolated, and genomic DNA was amplified by PCR (forward: 5′-CCCTCAGCTCCTCAGTTTCA-3′, reverse: 5′-CTCAGCCTGACTCTCACCTC-3′) followed by sequencing. Two independent ATP13A2-null HEK293 clones and two ATP13A2-null HeLa clones were selected for further analysis (Fig. S2, a and b).

Atp13a2-null (B6N.Cg-*Atp13a2*$^{tm1.1Pjsch}$/J) and C57BL/6 mice were obtained from Jackson Laboratory (Schultheis et al., 2013). Mice were housed in specific-pathogen–free facilities. The experimental protocol was approved by the Ethics Review Committee for Animal Experimentation of Central South University. Genotyping was conducted as described, with tail DNA (Schultheis et al., 2013). In brief, a 165-bp product from the WT allele and a 284-bp product from the mutant allele were amplified by PCR (Fig. S1 a). Primers were 5′-AACACTCCGTGCTTCAGTTTCC-3′ (forward), 5′-AAGGACACGGGACGCAAGCAG-3′ (reverse for WT allele), and 5′-CCAATACGCCCGCGTTTCTTCC-3′ (reverse for mutant allele).

Da-gal4, *Elav-gal4* (C155), and three *CG32000* RNAi lines were purchased from Bloomington Stock Center (TRiP.HMS05242 and TRiP.HMS02719) and Vienna Drosophila Resource Center (GD14627). Transgenic UAS-*d*HDAC6 WT and UAS-*d*HDAC6 H664A stocks were donated by Yongqing Zhang (Institute of Genetics and Developmental Biology, Chinese Academy of Sciences, Beijing, China; Xiong et al., 2013). All flies were maintained in standard cornmeal agar medium at 25°C.

Drug treatment

To test HDAC6 activity in vivo, we used inhibitor tubacin treatment followed by a chase experiment. Cells were incubated in complete culture medium containing 2 µM tubacin for 14 h to inhibit HDAC6, followed by removal of medium and replacement with tubacin-free medium. Cells were harvested at various time points, as indicated.

To assess aggresome clearance, cells were treated with 10 µM MG132 for 6 h, rinsed twice in PBS, and cultured in complete medium for indicated times. To inhibit HDAC6 in flies, Tubastatin A (150 µM) was mixed with *Drosophila* fast food. To induce autophagy, cells were either starved for 6 h (to induce general macroautophagy) or treated with CCCP (20 µM) for 6 h (to induce mitophagy). For experiments involving subcellular fractionation, mice were starved for 12 h with access only to water.

Cathepsin D activity assay

Cathepsin D activity assessed using a Cathepsin D activity assay kit (ab65302; Abcam) according to the manufacturer's protocol. In brief, 1 µg mouse cerebellum tissue or lysates containing 1.3 × 10^5 cells were assayed in 96-well plates. Tissue homogenates or cell lysates were centrifuged at 15,000 *g* for 5 min at 4°C to remove cell debris. Supernatants were incubated with the Cathepsin D substrate GKPILFFRLK(Dnp)-D-R-NH_2 labeled with MCA at 37°C for 1 h in the dark. Fluorescence was quantified with a fluorescence plate reader (Biotek) with excitation/emission of 328/460 nm.

Real-time PCR

Total RNA isolated using Trizol reagent (15596-018; Invitrogen) was converted to cDNA with the Verso cDNA Kit (AB1453B; Thermo Fisher Scientific) according to the manufacturer's instruction. SYBR Green qPCR Master Mix (2×; K0251; Thermo Fisher Scientific) was used for quantitative real-time PCR amplification with a CFX96 Real-Time PCR Detection System (Bio-Rad) and corresponding software (Applied Biosystems). Primers for

KO) HEK293 cells expressing ATP13A2 variants (WT, delC, F182L, or G504R) were immunodetected for LC3 (LC3-I, LC3-II), ATP13A2 variants (FLAG), or α-tubulin (α-tub). WT and ATP13A2-null HEK293 cells transfected with an empty plasmid (KO/Ctrl) served as controls (e). Quantitation of ac-tub/α-tub and LC3-II/α-tub ratio is shown (f and g; $n = 3$). ***, $P < 0.001$; ****, $P < 0.0001$. **(h)** ATP13A2 pathogenic mutants do not promote protein aggregate degradation in ATP13A2-null cells. ATP13A2-null (KO) MEFs expressing ATP13A2 variants (WT, delC, F182L, or G504R) were treated with MG132 for 12 h to induce protein aggregation, followed by removal of MG132. Immunostaining with an anti-ubiquitin antibody and an anti-V5 tag antibody was used on insoluble protein aggregates (green, Ubi) and ATP13A2 (red, V5, lower panel), respectively. Cells transfected with control empty plasmid served as negative controls (KO/Ctrl). Dashed lines outline transfectants. Bar, 7.5 µm.

dATP13A2 were 5′-CCCAATTCAAAAAATGCTCAT-3′ (forward) and 5′-TGTCTTGAAATCTCGCAATGGTA-3′ (reverse). PCR was performed with 1 cycle at 50°C for 2 min and 95°C for 10 min, followed by 40 cycles at 95°C, 15 s, and 60°C, 1 min. Gene expression was normalized to actin, and relative mRNA levels were calculated based on the comparative C_T method.

mtDNA quantification

WT and ATP13A2-null HEK293 cells were transfected with empty control vector or a plasmid encoding HDAC6, followed by CCCP treatment (20 µM) for 6 h. Total cellular DNA was extracted using the DNeasy Blood and Tissue kit (69506; Qiagen), according to the manufacturer's instructions. Relative mtDNA content was measured as described (Zhang et al., 2016). In brief, both mtDNA (measured by mitochondrial *16S rRNA* gene) and nuclear DNA (nDNA, measured by the β2-microglobulin gene) in the same experimental conditions were assessed by quantitative PCR with a CFX96 Real-Time PCR Detection System (Bio-Rad) with the SYBR GreenER qPCR SuperMix (11762-500; Thermo Fisher Scientific). The primers were *16S rRNA* gene: 5′-GCCTTCCCCCGTAAATGATA-3′ (forward), 5′-TTATGCGATTACCGGGCTCT-3′ (reverse); *β2-microglobulin*: 5′-TGCTGTCTCCATGTTTGATGTATCT-3′ (forward), 5′-TCTCTGCTCCCCACCTCTAAGT-3′ (reverse). C_T values were obtained automatically. The relative content of mtDNA in cells was shown as the ratio of mtDNA/nDNA, which was calculated by 2ΔCT. ΔC_T is the difference in C_T values between the β2-microglobulin gene and the 16S rRNA gene.

Mouse tissue preparation

18-mo-old male mice were anesthetized and transcardially perfused with prechilled PBS followed by ice-cold 4% PFA for prefixation. Liver (left lateral lobe) was transferred into 4% PFA for postfixation for 24 h. Samples were washed with PBS and dehydrated with either 30% sucrose solution at 4°C for optimal cutting temperature compound embedding or serial solutions of graded alcohol and xylene for paraffin embedding. Samples were frozen and sectioned at a thickness of 30 µm with a Leica cryostat. Paraffin-embedded samples were sectioned at a thickness of 10 µm on a Leica rotary microtome. Tissue slices were further stained by hematoxylin and eosin (H&E), Oil red O, or periodic acid Schiff, according to standard protocols.

Immunoassays

Immunoblot analysis, immunoprecipitation, and immunofluorescence were essentially performed as described (Xiong et al., 2009; Zhang et al., 2016). For coimmunoprecipitation, cell lysis buffer included 1% Triton X-100, 10 mM Hepes, pH 7.5, 142.5 mM KCl, 5 mM $MgCl_2$,1 mM EDTA, 10% glycerol, and a protease inhibitor cocktail. Proteins were separated on an SDS-PAGE gel, and quantitation was performed wih ImageJ software (National Institutes of Health). For immunofluorescence, nuclei were DAPI-stained (Sigma-Aldrich). Slides were mounted with Fluoroshield (Sigma-Aldrich). Liver tissue slices from five mice of each genotype were permeabilized with 0.3% PBST for 1 h at RT and blocked using 5% BSA in 0.3% PBS-Tween for 1 h at RT. These free-floating slices were incubated with an anti-p62/SQSTM1 (1:200) or anti-LC3 (1:200) antibody at 4°C overnight, followed by corresponding secondary antibodies for 2 h at RT. Nuclei were counterstained by DAPI.

LysoTracker and Magic Red cathepsin B assay

Fly eggs at stage 12–13 were dissected in prechilled PBS, pH 7.4. Samples were stained with LysoTracker Red DND99 (Thermo Fisher Scientific). Magic Red (ImmunoChemistry Technologies) staining was performed according to the manufacturer's instructions. Nuclei were stained with DAPI. Images were acquired with a scanning confocal microscope (TSC, SP5; Leica) with a Plan-Apochromat 100× NA 1.4 oil differential interference contrast objective lens. Quantification was performed with ImageJ software.

Drosophila climbing assay

The climbing assay was conducted as described (Wang et al., 2006; Zhang et al., 2016). In brief, groups of 15-d-old male flies were anesthetized with CO_2 and transferred into transparent plastic vials 25 cm in length and 1.5 cm in diameter. Flies were then rested for 30 min. Flies were tapped down to the bottom of the vial, and the time required for five flies to climb up to a 10-cm finish line was recorded. The climbing index is reported as speed (cm/s). The assay was repeated three times for each group with 5-min intervals. At least 100 flies of each genotype were tested, and the mean climbing time for each was calculated.

Detection of insoluble ubiquitinated proteins in fly heads and mouse tissues

60 male flies per group were frozen in liquid nitrogen and shaken vigorously. Fly heads and mouse liver tissues were collected and homogenized in 1% Triton X-100 in PBS containing a protease inhibitor cocktail and phosphatase inhibitors, followed by centrifugation at 12,000 *g* for 15 min at 4°C. The supernatant contained Triton X-100 soluble lysates. Cell debris was rinsed with 1% Triton X-100 in PBS three times and then homogenized in 2× SDS lysis buffer (63 mM Tris HCl, pH 6.8, 2% SDS, 10% glycerol, and protease inhibitor cocktail). After centrifugation at 15,000 *g* for 15 min at room temperature, the supernatant, which contains Triton X-100–insoluble lysates, was removed. Both lysates were separated on polyacrylamide gels and immunoblotted with an anti-ubiquitin antibody.

Subcellular fractionation and in vitro fusion assay

Subcellular fractionation was undertaken as described, with minor modifications (Wattiaux et al., 1978; Goldstein et al., 1983). In brief, livers of 5-mo-old mice were dissected and finely minced. Liver tissue was rinsed with prechilled PBS, resuspended in 7–8 ml homogenization solution (250 mM sucrose, 10 mM Hepes, pH 7.4, 1 mM EDTA, and protease inhibitor cocktail), and transferred to a Dounce homogenizer for homogenization with pestle type B, 15–20 strokes. Lysates were centrifuged at 1,000 *g* for 10 min at 4°C. The floating fat layer was removed, and the supernatant was saved. The pellet was resuspended in two volumes of homogenization solution and gently homogenized for another 3–4 strokes followed by centrifugation. Supernatants were combined and centrifuged at 20,000 *g* at 4°C for 20 min. Resulting supernatants were saved as the cytosolic fraction. The pellet was resuspended in 2.25 ml homogenization solution and mixed with 3.75 ml 80% (wt/vol)

Histodenz (Sigma-Aldrich) stock solution (80% Histodenz, 1 mM EDTA, and 10 mM Hepes, pH 7.4). A discontinuous Histodenz gradient (26%, 24%, 20%, and 15%) with protease inhibitor was carefully layered on top of the lysates, followed by centrifuging at 25,000 rpm at 4°C for 4 h. The APS and LYS fractions at the interfaces of gradients were collected by syringe. Fractions were diluted to 0.01 µg/µl protein in fusion buffer (10 mM Hepes, pH 7.0, 10 mM KCl, 1.5 mM $MgCl_2$, 1 mM DTT, 250 mM sucrose, and protease inhibitor cocktail; Koga et al., 2010). APS were labeled by an anti-LC3 antibody and CY3-conjugated secondary antibody, and LYSs were labeled with an anti-LAMP1 antibody and Alexa Fluor 488–conjugated secondary antibody. A fusion reaction was performed in an energy-regenerating system (3 mM ATP, 2 mM GTP, 2 mM $CaCl_2$, 8 mM phosphocreatine, 0.16 mg/ml creatine phosphokinase, and protease inhibitor cocktail) at 37°C for 40 min. The vesicles in the no-energy group were supplied without ATP, GTP, and creatine phosphokinase. The vesicles in the bafilomycin A1 and tubacin groups were pretreated with chemicals for 20 min ahead of the reaction. The reaction was stopped by 8% PFA on ice for 15 min. Reaction mixtures were mounted on slides with 50% glycerol. All images were acquired by the scanning confocal microscope (TCS, SP5; Leica) with a Plan-Apochromat 100× NA 1.4 oil differential interference contrast objective lens equipped with a high-speed CCD camera (DFC310 FX; Leica) and running Leica Application Suite software (LAS v.2.7.2) at room temperature. Images were edited using Photoshop 7.0 (Adobe) and assembled with Illustrator 10 (Adobe). Fusion events were quantified by ImageJ and expressed as a percentage of total vesicles. Colocalization was analyzed using JACoP plugin software (National Institutes of Health).

In vitro HDAC6 activity assay

The HDAC6 activity assay was conducted according to the manual (HDAC6 Fluorimetric Drug Discovery Kit, BML-AK516; Enzo Life Sciences) with minor modifications. In brief, the lysosomal and mitochondrial fractions from WT and ATP13A2 knockout mouse livers were isolated using the method describe in the previous paragraph and diluted with HDAC6 Assay Buffer II (BML-KI422-0020; Enzo Life Sciences) supplemented with 250 mM sucrose to maintain lysosomal integrity. The cytoplasmic components were saved after the crude centrifugation at 20,000 *g* for 20 min at 4°C. Beyond that, the HDAC Assay Buffer should also be supplemented with 250 mM sucrose for further analysis. 20-µg relative lysosomal and mitochondrial fractions or 10 µg of cytoplasmic components were loaded into the reaction system. The reaction was conducted basically according to the manual. The final concentration of trichostatin A (BML-GR309-9090; Enzo Life Sciences) in the reaction system was 20 µM. The fluorescence was recorded at 0, 15, 30, and 60 min by a fluorescence plate reader (Biotek) with excitation/emission of 328/460 nm.

TEM

Cells in culture were either starved for 6 h (for LYS analysis) or treated with CCCP (20 µM) for 6 h (for mitophagy analysis) followed by fixation in 2.5% glutaraldehyde at 4°C overnight. Fly brain tissues (3- and 30-d-old) and mouse brain tissues were dissected and fixed in 2.5% glutaraldehyde at 4°C overnight. Subcellular fractions were fixed in 2.5% glutaraldehyde at RT for 1 h. All samples were postfixed in 2% OsO_4 (Electron Microscopy Sciences). After dehydration with a graded series of acetones, samples were infiltrated in acetone/resin (1:1) and embedded in Epon (Sigma-Aldrich). Slides of ultrathin sections (70 nm) were double stained with uranyl acetate (Ted Pella) and lead nitrate (Sigma-Aldrich). Images were taken by using the transmission electron microscope Tecnai G2 Spirit (Thermo Fisher Scientific) equipped with an Eagle 4k HS digital camera.

Statistical analysis

Statistical analysis was performed with Prism 5 software (GraphPad). Two-tailed Student's *t*-test was used to determine the difference between two groups. Statistical significance between multiple groups was performed with one-way ANOVA followed by Tukey's test. One-way ANOVA with Dunnett's tests wase used to assess differences between treatment groups and their controls. Error bars indicate ±SD. Quantitation was performed by double-blinded experimenters.

Online supplemental material

Fig. S1 shows characterization of the ATP13A2-deficiency mouse line and ATP13A2-deficiency cell lines. Fig. S2 shows TEM analysis of ATP13A2-null mouse brain tissues. Fig. S3 shows that HDAC6 is a major deacetylase for α-tubulin in both HEK293 cells and *Drosophila*. Fig. S4 shows characterization of HDAC6 activity in ATP13A2-null cells and on LYS of ATP13A2-null mice. Fig. S5 shows functional analysis of ATP13A2 deficiency.

Acknowledgments

We thank Dr. Yongqing Zhang for providing *d*HDAC6 transgenic flies and Dr. Christian Kubisch for plasmids encoding ATP13A2 WT and delC mutant.

This work was supported by grants from the National Natural Science Foundation of China (31330031, 31730036, 81861138012, 81429002, and 81161120498), the Discipline Innovative Engineering Plan of China (111 Program), a key laboratory grant from Hunan Province (2016TP1006), and a grant from the National Key Plan for Scientific Research and Development of China (2016YFC1306000).

The authors declare no competing financial interests.

Author contributions: The project was originally conceived by Z. Zhang. Experiments were performed by R. Wang, J. Tan, T. Chen, H. Han, R. Tian, Y. Tan, Y. Wu, J. Cui, F. Chen, J. Li, L. Lv, X. Guan, and S. Shang. J. Tan, J. Lu, and Z. Zhang provided intellectual input. R. Wang, J. Tan, T. Chen, and Z. Zhang wrote the manuscript.

Submitted: 24 April 2018
Revised: 28 August 2018
Accepted: 29 October 2018

References

Bánréti, A., M. Sass, and Y. Graba. 2013. The emerging role of acetylation in the regulation of autophagy. *Autophagy.* 9:819–829. https://doi.org/10.4161/auto.23908

Behrens, M.I., N. Brüggemann, P. Chana, P. Venegas, M. Kägi, T. Parrao, P. Orellana, C. Garrido, C.V. Rojas, J. Hauke, et al. 2010. Clinical spectrum of Kufor-Rakeb syndrome in the Chilean kindred with ATP13A2 mutations. *Mov. Disord.* 25:1929–1937. https://doi.org/10.1002/mds.22996

Bento, C.F., A. Ashkenazi, M. Jimenez-Sanchez, and D.C. Rubinsztein. 2016a. The Parkinson's disease-associated genes ATP13A2 and SYT11 regulate autophagy via a common pathway. *Nat. Commun.* 7:11803. https://doi.org/10.1038/ncomms11803

Bento, C.F., M. Renna, G. Ghislat, C. Puri, A. Ashkenazi, M. Vicinanza, F.M. Menzies, and D.C. Rubinsztein. 2016b. Mammalian autophagy: How does it work? *Annu. Rev. Biochem.* 85:685–713. https://doi.org/10.1146/annurev-biochem-060815-014556

Boyault, C., B. Gilquin, Y. Zhang, V. Rybin, E. Garman, W. Meyer-Klaucke, P. Matthias, C.W. Müller, and S. Khochbin. 2006. HDAC6-p97/VCP controlled polyubiquitin chain turnover. *EMBO J.* 25:3357–3366. https://doi.org/10.1038/sj.emboj.7601210

Bras, J., A. Verloes, S.A. Schneider, S.E. Mole, and R.J. Guerreiro. 2012. Mutation of the parkinsonism gene ATP13A2 causes neuronal ceroid-lipofuscinosis. *Hum. Mol. Genet.* 21:2646–2650. https://doi.org/10.1093/hmg/dds089

Dehay, B., A. Ramirez, M. Martinez-Vicente, C. Perier, M.H. Canron, E. Doudnikoff, A. Vital, M. Vila, C. Klein, and E. Bezard. 2012. Loss of P-type ATPase ATP13A2/PARK9 function induces general lysosomal deficiency and leads to Parkinson disease neurodegeneration. *Proc. Natl. Acad. Sci. USA.* 109:9611–9616. https://doi.org/10.1073/pnas.1112368109

Di Fonzo, A., H.F. Chien, M. Socal, S. Giraudo, C. Tassorelli, G. Iliceto, G. Fabbrini, R. Marconi, E. Fincati, G. Abbruzzese, et al. Italian Parkinson Genetics Network. 2007. ATP13A2 missense mutations in juvenile parkinsonism and young onset Parkinson disease. *Neurology.* 68:1557–1562. https://doi.org/10.1212/01.wnl.0000260963.08711.08

Djarmati, A., J. Hagenah, K. Reetz, S. Winkler, M.I. Behrens, H. Pawlack, K. Lohmann, A. Ramirez, V. Tadić, N. Brüggemann, 2009. ATP13A2 variants in early-onset Parkinson's disease patients and controls. *Mov. Disord.* 24:2104–2111. https://doi.org/10.1002/mds.22728

Estrada-Cuzcano, A., S. Martin, T. Chamova, M. Synofzik, D. Timmann, T. Holemans, A. Andreeva, J. Reichbauer, R. De Rycke, D.I. Chang, et al. 2017. Loss-of-function mutations in the ATP13A2/PARK9 gene cause complicated hereditary spastic paraplegia (SPG78). *Brain.* 140:287–305. https://doi.org/10.1093/brain/aww307

Gitler, A.D., A. Chesi, M.L. Geddie, K.E. Strathearn, S. Hamamichi, K.J. Hill, K.A. Caldwell, G.A. Caldwell, A.A. Cooper, J.C. Rochet, and S. Lindquist. 2009. Alpha-synuclein is part of a diverse and highly conserved interaction network that includes PARK9 and manganese toxicity. *Nat. Genet.* 41:308–315. https://doi.org/10.1038/ng.300

Goldstein, J.L., S.K. Basu, and M.S. Brown. 1983. Receptor-mediated endocytosis of low-density lipoprotein in cultured cells. *Methods Enzymol.* 98:241–260. https://doi.org/10.1016/0076-6879(83)98152-1

Grünewald, A., B. Arns, P. Seibler, A. Rakovic, A. Münchau, A. Ramirez, C.M. Sue, and C. Klein. 2012. ATP13A2 mutations impair mitochondrial function in fibroblasts from patients with Kufor-Rakeb syndrome. *Neurobiol. Aging.* 33:1843.e1–1843.e7. https://doi.org/10.1016/j.neurobiolaging.2011.12.035

Gusdon, A.M., J. Zhu, B. Van Houten, and C.T. Chu. 2012. ATP13A2 regulates mitochondrial bioenergetics through macroautophagy. *Neurobiol. Dis.* 45:962–972. https://doi.org/10.1016/j.nbd.2011.12.015

Hao, R., P. Nanduri, Y. Rao, R.S. Panichelli, A. Ito, M. Yoshida, and T.P. Yao. 2013. Proteasomes activate aggresome disassembly and clearance by producing unanchored ubiquitin chains. *Mol. Cell.* 51:819–828. https://doi.org/10.1016/j.molcel.2013.08.016

Hasegawa, J., R. Iwamoto, T. Otomo, A. Nezu, M. Hamasaki, and T. Yoshimori. 2016. Autophagosome-lysosome fusion in neurons requires INPP5E, a protein associated with Joubert syndrome. *EMBO J.* 35:1853–1867. https://doi.org/10.15252/embj.201593148

Hubbert, C., A. Guardiola, R. Shao, Y. Kawaguchi, A. Ito, A. Nixon, M. Yoshida, X.F. Wang, and T.P. Yao. 2002. HDAC6 is a microtubule-associated deacetylase. *Nature.* 417:455–458. https://doi.org/10.1038/417455a

Jaber, N., Z. Dou, J.S. Chen, J. Catanzaro, Y.P. Jiang, L.M. Ballou, E. Selinger, X. Ouyang, R.Z. Lin, J. Zhang, and W.X. Zong. 2012. Class III PI3K Vps34 plays an essential role in autophagy and in heart and liver function. *Proc. Natl. Acad. Sci. USA.* 109:2003–2008. https://doi.org/10.1073/pnas.1112848109

Jiang, P., and N. Mizushima. 2014. Autophagy and human diseases. *Cell Res.* 24:69–79. https://doi.org/10.1038/cr.2013.161

Kett, L.R., B. Stiller, M.M. Bernath, I. Tasset, J. Blesa, V. Jackson-Lewis, R.B. Chan, B. Zhou, G. Di Paolo, S. Przedborski, et al. 2015. α-Synuclein-independent histopathological and motor deficits in mice lacking the endolysosomal Parkinsonism protein Atp13a2. *J. Neurosci.* 35:5724–5742. https://doi.org/10.1523/JNEUROSCI.0632-14.2015

Kimura, S., T. Noda, and T. Yoshimori. 2007. Dissection of the autophagosome maturation process by a novel reporter protein, tandem fluorescent-tagged LC3. *Autophagy.* 3:452–460. https://doi.org/10.4161/auto.4451

Koga, H., S. Kaushik, and A.M. Cuervo. 2010. Altered lipid content inhibits autophagic vesicular fusion. *FASEB J.* 24:3052–3065. https://doi.org/10.1096/fj.09-144519

Komatsu, M., S. Waguri, T. Ueno, J. Iwata, S. Murata, I. Tanida, J. Ezaki, N. Mizushima, Y. Ohsumi, Y. Uchiyama, et al. 2005. Impairment of starvation-induced and constitutive autophagy in Atg7-deficient mice. *J. Cell Biol.* 169:425–434. https://doi.org/10.1083/jcb.200412022

Kong, S.M., B.K. Chan, J.S. Park, K.J. Hill, J.B. Aitken, L. Cottle, H. Farghaian, A.R. Cole, P.A. Lay, C.M. Sue, and A.A. Cooper. 2014. Parkinson's disease-linked human PARK9/ATP13A2 maintains zinc homeostasis and promotes α-Synuclein externalization via exosomes. *Hum. Mol. Genet.* 23:2816–2833. https://doi.org/10.1093/hmg/ddu099

Lamb, C.A., T. Yoshimori, and S.A. Tooze. 2013. The autophagosome: origins unknown, biogenesis complex. *Nat. Rev. Mol. Cell Biol.* 14:759–774. https://doi.org/10.1038/nrm3696

Lee, J.Y., H. Koga, Y. Kawaguchi, W. Tang, E. Wong, Y.S. Gao, U.B. Pandey, S. Kaushik, E. Tresse, J. Lu, et al. 2010. HDAC6 controls autophagosome maturation essential for ubiquitin-selective quality-control autophagy. *EMBO J.* 29:969–980. https://doi.org/10.1038/emboj.2009.405

Lees, A.J., and A.B. Singleton. 2007. Clinical heterogeneity of ATP13A2 linked disease (Kufor-Rakeb) justifies a PARK designation. *Neurology.* 68:1553–1554. https://doi.org/10.1212/01.wnl.0000265228.66664.f4

Levine, B., and G. Kroemer. 2008. Autophagy in the pathogenesis of disease. *Cell.* 132:27–42. https://doi.org/10.1016/j.cell.2007.12.018

Lin, C.H., E.K. Tan, M.L. Chen, L.C. Tan, H.Q. Lim, G.S. Chen, and R.M. Wu. 2008. Novel ATP13A2 variant associated with Parkinson disease in Taiwan and Singapore. *Neurology.* 71:1727–1732. https://doi.org/10.1212/01.wnl.0000335167.72412.68

Mao, X.Y., J.M. Burgunder, Z.J. Zhang, X.L. Chang, R. Peng, J.M. Burgunder, Y. Yang, Y.C. Wang, T. Li, and Z.J. Zhang. 2010. ATP13A2 G2236A variant is rare in patients with early-onset Parkinson's disease and familial Parkinson's disease from Mainland China. *Parkinsonism Relat. Disord.* 16:235–236. https://doi.org/10.1016/j.parkreldis.2009.11.010

Matsui, H., F. Sato, S. Sato, M. Koike, Y. Taruno, S. Saiki, M. Funayama, H. Ito, Y. Taniguchi, N. Uemura, et al. 2013. ATP13A2 deficiency induces a decrease in cathepsin D activity, fingerprint-like inclusion body formation, and selective degeneration of dopaminergic neurons. *FEBS Lett.* 587:1316–1325. https://doi.org/10.1016/j.febslet.2013.02.046

Mizushima, N., T. Yoshimori, and Y. Ohsumi. 2011. The role of Atg proteins in autophagosome formation. *Annu. Rev. Cell Dev. Biol.* 27:107–132. https://doi.org/10.1146/annurev-cellbio-092910-154005

Najim al-Din, A.S., A. Wriekat, A. Mubaidin, M. Dasouki, and M. Hiari. 1994. Pallido-pyramidal degeneration, supranuclear upgaze paresis and dementia: Kufor-Rakeb syndrome. *Acta Neurol. Scand.* 89:347–352. https://doi.org/10.1111/j.1600-0404.1994.tb02645.x

Ni, H.M., N. Boggess, M.R. McGill, M. Lebofsky, P. Borude, U. Apte, H. Jaeschke, and W.X. Ding. 2012. Liver-specific loss of Atg5 causes persistent activation of Nrf2 and protects against acetaminophen-induced liver injury. *Toxicol. Sci.* 127:438–450. https://doi.org/10.1093/toxsci/kfs133

Ning, Y.P., K. Kanai, H. Tomiyama, Y. Li, M. Funayama, H. Yoshino, S. Sato, M. Asahina, S. Kuwabara, A. Takeda, et al. 2008. PARK9-linked parkinsonism in eastern Asia: mutation detection in ATP13A2 and clinical phenotype. *Neurology.* 70:1491–1493. https://doi.org/10.1212/01.wnl.0000310427.72236.68

North, B.J., B.L. Marshall, M.T. Borra, J.M. Denu, and E. Verdin. 2003. The human Sir2 ortholog, SIRT2, is an NAD+-dependent tubulin deacetylase. *Mol. Cell.* 11:437–444. https://doi.org/10.1016/S1097-2765(03)00038-8

Park, J.S., B. Koentjoro, D. Veivers, A. Mackay-Sim, and C.M. Sue. 2014. Parkinson's disease-associated human ATP13A2 (PARK9) deficiency causes zinc dyshomeostasis and mitochondrial dysfunction. *Hum. Mol. Genet.* 23:2802–2815. https://doi.org/10.1093/hmg/ddt623

Radi, E., P. Formichi, G. Di Maio, C. Battisti, and A. Federico. 2012. Altered apoptosis regulation in Kufor-Rakeb syndrome patients with mutations in the ATP13A2 gene. *J. Cell. Mol. Med.* 16:1916–1923.

Ramirez, A., A. Heimbach, J. Gründemann, B. Stiller, D. Hampshire, L.P. Cid, I. Goebel, A.F. Mubaidin, A.L. Wriekat, J. Roeper, et al. 2006. Hereditary parkinsonism with dementia is caused by mutations in ATP13A2, encoding a lysosomal type 5 P-type ATPase. *Nat. Genet.* 38:1184–1191. https://doi.org/10.1038/ng1884

Sanjana, N.E., O. Shalem, and F. Zhang. 2014. Improved vectors and genome-wide libraries for CRISPR screening. *Nat. Methods.* 11:783–784. https://doi.org/10.1038/nmeth.3047

Santoro, L., G.J. Breedveld, F. Manganelli, R. Iodice, C. Pisciotta, M. Nolano, F. Punzo, M. Quarantelli, S. Pappatà, A. Di Fonzo, et al. 2011. Novel ATP13A2 (PARK9) homozygous mutation in a family with marked phenotype variability. *Neurogenetics.* 12:33–39. https://doi.org/10.1007/s10048-010-0259-0

Sato, S., M. Koike, M. Funayama, J. Ezaki, T. Fukuda, T. Ueno, Y. Uchiyama, and N. Hattori. 2016. Lysosomal Storage of Subunit c of Mitochondrial ATP Synthase in Brain-Specific Atp13a2-Deficient Mice. *Am. J. Pathol.* 186:3074–3082. https://doi.org/10.1016/j.ajpath.2016.08.006

Schneider, S.A., C. Paisan-Ruiz, N.P. Quinn, A.J. Lees, H. Houlden, J. Hardy, and K.P. Bhatia. 2010. ATP13A2 mutations (PARK9) cause neurodegeneration with brain iron accumulation. *Mov. Disord.* 25:979–984. https://doi.org/10.1002/mds.22947

Schultheis, P.J., S.M. Fleming, A.K. Clippinger, J. Lewis, T. Tsunemi, B. Giasson, D.W. Dickson, J.R. Mazzulli, M.E. Bardgett, K.L. Haik, et al. 2013. Atp13a2-deficient mice exhibit neuronal ceroid lipofuscinosis, limited α-synuclein accumulation and age-dependent sensorimotor deficits. *Hum. Mol. Genet.* 22:2067–2082. https://doi.org/10.1093/hmg/ddt057

Settembre, C., R. De Cegli, G. Mansueto, P.K. Saha, F. Vetrini, O. Visvikis, T. Huynh, A. Carissimo, D. Palmer, T.J. Klisch, et al. 2013. TFEB controls cellular lipid metabolism through a starvation-induced autoregulatory loop. *Nat. Cell Biol.* 15:647–658. https://doi.org/10.1038/ncb2718

Shalem, O., N.E. Sanjana, E. Hartenian, X. Shi, D.A. Scott, T. Mikkelson, D. Heckl, B.L. Ebert, D.E. Root, J.G. Doench, and F. Zhang. 2014. Genome-scale CRISPR-Cas9 knockout screening in human cells. *Science.* 343:84–87. https://doi.org/10.1126/science.1247005

Shen, H.M., and N. Mizushima. 2014. At the end of the autophagic road: an emerging understanding of lysosomal functions in autophagy. *Trends Biochem. Sci.* 39:61–71. https://doi.org/10.1016/j.tibs.2013.12.001

Singh, R., Y. Xiang, Y. Wang, K. Baikati, A.M. Cuervo, Y.K. Luu, Y. Tang, J.E. Pessin, G.J. Schwartz, and M.J. Czaja. 2009. Autophagy regulates adipose mass and differentiation in mice. *J. Clin. Invest.* 119:3329–3339.

Tan, J., T. Zhang, L. Jiang, J. Chi, D. Hu, Q. Pan, D. Wang, and Z. Zhang. 2011. Regulation of intracellular manganese homeostasis by Kufor-Rakeb syndrome-associated ATP13A2 protein. *J. Biol. Chem.* 286:29654–29662. https://doi.org/10.1074/jbc.M111.233874

Tsunemi, T., and D. Krainc. 2014. Zn^{2+} dyshomeostasis caused by loss of ATP13A2/PARK9 leads to lysosomal dysfunction and alpha-synuclein accumulation. *Hum. Mol. Genet.* 23:2791–2801. https://doi.org/10.1093/hmg/ddt572

Ugolino, J., S. Fang, C. Kubisch, and M.J. Monteiro. 2011. Mutant Atp13a2 proteins involved in parkinsonism are degraded by ER-associated degradation and sensitize cells to ER-stress induced cell death. *Hum. Mol. Genet.* 20:3565–3577. https://doi.org/10.1093/hmg/ddr274

Usenovic, M., and D. Krainc. 2012. Lysosomal dysfunction in neurodegeneration: the role of ATP13A2/PARK9. *Autophagy.* 8:987–988. https://doi.org/10.4161/auto.20256

Usenovic, M., A.L. Knight, A. Ray, V. Wong, K.R. Brown, G.A. Caldwell, K.A. Caldwell, I. Stagljar, and D. Krainc. 2012a. Identification of novel ATP13A2 interactors and their role in α-synuclein misfolding and toxicity. *Hum. Mol. Genet.* 21:3785–3794. https://doi.org/10.1093/hmg/dds206

Usenovic, M., E. Tresse, J.R. Mazzulli, J.P. Taylor, and D. Krainc. 2012b. Deficiency of ATP13A2 leads to lysosomal dysfunction, α-synuclein accumulation, and neurotoxicity. *J. Neurosci.* 32:4240–4246. https://doi.org/10.1523/JNEUROSCI.5575-11.2012

Wang, D., L. Qian, H. Xiong, J. Liu, W.S. Neckameyer, S. Oldham, K. Xia, J. Wang, R. Bodmer, and Z. Zhang. 2006. Antioxidants protect PINK1-dependent dopaminergic neurons in Drosophila. *Proc. Natl. Acad. Sci. USA.* 103:13520–13525. https://doi.org/10.1073/pnas.0604661103

Wang, Z., G. Miao, X. Xue, X. Guo, C. Yuan, Z. Wang, G. Zhang, Y. Chen, D. Feng, J. Hu, and H. Zhang. 2016. The Vici Syndrome Protein EPG5 Is a Rab7 Effector that Determines the Fusion Specificity of Autophagosomes with Late Endosomes/Lysosomes. *Mol. Cell.* 63:781–795. https://doi.org/10.1016/j.molcel.2016.08.021

Wattiaux, R., S. Wattiaux-De Coninck, M.F. Ronveaux-dupal, and F. Dubois. 1978. Isolation of rat liver lysosomes by isopycnic centrifugation in a metrizamide gradient. *J. Cell Biol.* 78:349–368. https://doi.org/10.1083/jcb.78.2.349

Xia, Q., H. Wang, Z. Hao, C. Fu, Q. Hu, F. Gao, H. Ren, D. Chen, J. Han, Z. Ying, and G. Wang. 2016. TDP-43 loss of function increases TFEB activity and blocks autophagosome-lysosome fusion. *EMBO J.* 35:121–142. https://doi.org/10.15252/embj.201591998

Xiong, H., D. Wang, L. Chen, Y.S. Choo, H. Ma, C. Tang, K. Xia, W. Jiang, Z. Ronai, X. Zhuang, and Z. Zhang. 2009. Parkin, PINK1, and DJ-1 form a ubiquitin E3 ligase complex promoting unfolded protein degradation. *J. Clin. Invest.* 119:650–660. https://doi.org/10.1172/JCI37617

Xiong, Y., K. Zhao, J. Wu, Z. Xu, S. Jin, and Y.Q. Zhang. 2013. HDAC6 mutations rescue human tau-induced microtubule defects in Drosophila. *Proc. Natl. Acad. Sci. USA.* 110:4604–4609. https://doi.org/10.1073/pnas.1207586110

Zhang, T., L. Xue, L. Li, C. Tang, Z. Wan, R. Wang, J. Tan, Y. Tan, H. Han, R. Tian, et al. 2016. BNIP3 Protein Suppresses PINK1 Kinase Proteolytic Cleavage to Promote Mitophagy. *J. Biol. Chem.* 291:21616–21629. https://doi.org/10.1074/jbc.M116.733410

Zhang, X., Z. Yuan, Y. Zhang, S. Yong, A. Salas-Burgos, J. Koomen, N. Olashaw, J.T. Parsons, X.J. Yang, S.R. Dent, et al. 2007. HDAC6 modulates cell motility by altering the acetylation level of cortactin. *Mol. Cell.* 27:197–213. https://doi.org/10.1016/j.molcel.2007.05.033

Zhang, Y., S. Goldman, R. Baerga, Y. Zhao, M. Komatsu, and S. Jin. 2009. Adipose-specific deletion of autophagy-related gene 7 (atg7) in mice reveals a role in adipogenesis. *Proc. Natl. Acad. Sci. USA.* 106:19860–19865. https://doi.org/10.1073/pnas.0906048106

Zhao, Y.G., H. Zhao, L. Miao, L. Wang, F. Sun, and H. Zhang. 2012. The p53-induced gene Ei24 is an essential component of the basal autophagy pathway. *J. Biol. Chem.* 287:42053–42063. https://doi.org/10.1074/jbc.M112.415968

Zou, H., Y. Wu, M. Navre, and B.C. Sang. 2006. Characterization of the two catalytic domains in histone deacetylase 6. *Biochem. Biophys. Res. Commun.* 341:45–50. https://doi.org/10.1016/j.bbrc.2005.12.144